

HUMAN ROBOT INTERACTION WITH 3D-PRINTED WHOLE BODY ROBOTIC
SKIN
by

FAHAD MIRZA

Presented to the Faculty of the Graduate School of
The University of Texas at Arlington in Partial Fulfillment
of the Requirements
for the Degree of

MASTER OF SCIENCE IN ELECTRICAL ENGINEERING

THE UNIVERSITY OF TEXAS AT ARLINGTON

May 2016

Copyright © by Fahad Mirza 2016

All Rights Reserved



ACKNOWLEDGEMENTS

First, I like to thank Dr. Dan O. Popa, my supervising professor for his constant guidance, support and the knowledge and wisdom he has imparted upon me. I will be forever in his debt for being there during my hard times. I believe a great part of my success is due to his mentorship. I like to express my gratitude to Dr. Woo Ho Lee for providing valuable advice into my research along the way. I would also like to thank Dr. Jason H. Losh for the courses he taught us and for providing insights about my research goal. Much appreciation also goes to Dr. Frank L. Lewis for taking an interest in my research and taking the time to serve on my thesis committee.

Next Gen System and its people will always have an influence in my life. I like to thank Isura Rantunga, who introduced me to NGS. The passion he holds for his work inspires me until these days. Namrata Balakrishnan, Yathartha Tuladhar, Sumit Kumar Das, Rommel Alonzo, Ruoshi Zhang and Sven Cremer are more than my colleagues. Their interesting company made my time at NGS enjoyable and worthwhile. I like to thank Joshua Baptist and Ritvij Sahasrabuddhe for their collaboration in my research.

My sincere gratitude goes to my wife Nafsia Matin, who flew all the way from Bangladesh to support me and to Ziaur Rahman for being there for me from the 1st day of my life in USA. I would also like to thank Reshmeen Silvia and my childhood friends Rupam Chowdhury and Tarique Nomani, for their mental support. A big shout-out to my brother Saeed Mirza and my sister Fatema Mirza for being the best siblings I could wish for, and to my mom Nargis Akter, for giving me the opportunity to follow my dreams. All my success belongs to her. Most of all I like to thank my creator, Allah. Without his blessings, I would not be here where I am today.

April 13, 2016

Abstract

HUMAN ROBOT INTERACTION WITH ROBOTIC SKIN

Fahad Mirza, MS

The University of Texas at Arlington, 2016

Supervising Professor: Dan O. Popa

This thesis presents work of a newly developed pressure sensor for robot skin, from fabrication to application. Robot skin, similar to human skin, is meant to have several sensing capabilities including pressure, temperature etc. As the conventional semiconductor manufacturing process is not adequate for multi-modal sensors, a new process called Electro-Hydro-Dynamic Printing has been explored in this work. A calibration technique was implemented along with printing parameter fixation by trial and error. A testing methodology was proposed to test these sensors and several commercial robots were used to conduct pHRI experiments with pressure sensing capability.

Table of Contents

ACKNOWLEDGEMENTS.....	iii
Abstract.....	iv
List of Illustrations	viii
List of Tables.....	xi
Chapter 1 Introduction	12
1.1 Motivation	12
1.2 Challenges	13
1.3 Contributions of this thesis.....	15
1.4 Thesis Organization	16
1.5 List of Publication	16
1.5.1 Conference Papers.....	16
Chapter 2 Background and Literature Survey.....	18
2.1 Characteristics of Human Skin	18
2.2 Research on Robot Skin.....	19
2.3 Robot Skin Sensor Manufacturing Technology.....	22
Chapter 3 Manufacturing of Pressure Sensors for Robot Skins.....	24
3.1 EHD as Printing Technology for Pressure Sensor Arrays.....	25
3.1.1 EHD Inkjet Printing.....	25
3.1.2 Pressure Sensor.....	26
3.1.3 Ink Formulation.....	29
3.1.4 Printing Parameter Optimization	31
3.1.5 Printing Calibration	34
3.2 Printing of Sensor Arrays	38
3.3 Packaging and Interconnection of Sensors.....	39

3.4 Interfacing with Electronics	40
3.4.1 Wheatstone Bridge.....	42
3.4.2 Instrumentation Amplifier	43
3.4.3 Butterworth filter	44
In this work, a Butterworth filter circuit was designed and implemented for pressure sensor signal conditioning after amplification.	46
3.4.4 Single sensor interfacing.....	46
3.4.5 Sensor Array interfacing - SkinCell.....	47
Chapter 4 Experimental Results	50
4.1 Testing Hardware	50
4.2 Experimental Results	54
4.2.1 Temperature Sensitivity.....	54
4.2.2 Humidity Sensitivity.....	58
4.2.3 Contact Pressure	60
4.2.4 Repeatability.....	61
4.2.5 Noise Sensitivity.....	62
4.2.6 Linearity.....	64
4.2.7 Thermal Drift.....	65
4.2.8 Crosstalk between structures	66
4.2.9 AC Response.....	67
Chapter 5 Applications to Robotics and Prosthetics.....	70
5.1 YouBot – A Mobile Manipulator with HRI.....	70
5.1.1 Sensors	72
5.1.1.1 IR Sensors.....	72
5.1.1.2 Interfacing IR sensors	73

5.1.1.3 Pressure Sensors.....	75
5.1.1.4 Interfacing Pressure Sensors.....	76
5.1.2 Casing.....	77
5.1.3 Real-Time Hardware.....	79
5.1.4 Software Framework.....	80
5.1.5 Guidance Experiments	81
5.2 RoboLimb – A Prosthetic Hand.....	86
5.2.1 Hardware Setup.....	86
5.2.2 Testing and Results.....	87
Chapter 6	89
6.1 Conclusion.....	89
6.1.1 Sensor Manufacturing Technology	89
6.1.2 Automated Printing	89
6.1.3 Sensor Characterization Methodology	90
6.1.4 Pressure Sensor Application on Robots	90
6.2 Future Work	90
6.2.1 Sensor Manufacturing Optimization	90
6.2.2 Automated Printing	91
6.2.3 Sensor Testing Methodology	91
6.2.4 Sensor's Application on Robots.....	91
References	92
Biographical Information.....	97

List of Illustrations

Figure 2-1 (a) Ballerina dancing with arm [51] (b) HEX-O-SKIN [52]	20
Figure 2-2 (a) Roboskin front and back view [53] (b) Roboskin patch [53]	21
Figure 2-3 Strip of TakkTile pressure sensor [55]	22
Figure 3-1 Sensor manufacturing steps	25
Figure 3-2 EHD Printing Setup	26
Figure 3-3 (a) IDE Structure made of Gold on Kapton Sheet (b) Dimensions (mm).....	28
Figure 3-4 Photograph showing the printing nozzle, and ink meniscus above an IDE structure	29
Figure 3-5 (a) Ohaus analytical scale (b) Sonifier.....	30
Figure 3-6 (a) Alicat Pressure Pump (b) 32 Gauge Nozzle	31
Figure 3-7 Hirox Microscope.....	33
Figure 3-8 Sample DMSO ink print with 800 μ m Nozzle Height, 0.9kV, 1kPa.....	33
Figure 3-9 Sample NMP ink print with 50mm/min, 0.95KV, 1kPa	34
Figure 3-10 Local and Global coordinate frames [31]	35
Figure 3-11 Vector representation of the calibration points [31]	Error! Bookmark not defined.
Figure 3-12 Local coordinates (mm)	36
Figure 3-13 Aerotech A3200 System [36]	36
Figure 3-14 (a) Front panel of the program (b) Printing trajectory	38
Figure 3-15 Sensor Array showing 16 tactels & corresponding 32 interconnect lines.	38
Figure 3-16 (a) Sensor encasing (b) An example of encasing.....	39
Figure 3-17 Patterned ZIF contact pads. 250x2500 μ m with a 500 μ m pitch	40
Figure 3-18 Change in resistance with strain for various materials [32]	42

Figure 3-19 Wheatstone bridge circuit [33].....	43
Figure 3-20 Instrumentational Amplifier schematic [34]	44
Figure 3-21 Frequency response of Butterworth LP filter from order 1 through 5 [35].....	45
Figure 3-22 Unity gain Butterworth LP filter with Sallen-Key topology [37]	46
Figure 3-23 Single sensor interfacing board.....	47
Figure 3-24 Block diagram of SkinCell.....	48
Figure 3-25 sensor array connected with the SkinCell.....	49
Figure 4-1 NI cRIO-9074 [61]	50
Figure 4-2 Functional block diagram of hardware setup	51
Figure 4-3 Experimental Setup.....	51
Figure 4-4 Tip Dimension	52
Figure 4-5 Temperature and humidity effect test setup.....	53
Figure 4-6 Temperature and humidity effect test setup.....	53
Figure 4-7 Variation of the sensor response with increasing temperature	54
Figure 4-8 Variation of the sensor response with decreasing temperature	55
Figure 4-9 Variation of the sensor response with return to room temperature.....	55
Figure 4-10 Sensor 2 response with increasing temp.....	56
Figure 4-11 Sensor 2 response with return to room temperature	56
Figure 4-12 Sensor response Vs temperature	57
Figure 4-13 Sensor 1 response with change of humidity	58
Figure 4-14 Sensor 2 response with change of humidity	59
Figure 4-15 Sensor array with markings	60
Figure 4-16 Repeatability test results	61
Figure 4-17 Structure 16 SNR calculation	63
Figure 4-18 Linearity test	64

Figure 4-19 Hysteresis effect	65
Figure 4-20 Thermal Drift	66
Figure 4-21 Crosstalk between sensors	67
Figure 4-23 Ac response of structure 1	68
Figure 4-24 Ac response of structure 6	68
Figure 4-25 Ac response of structure 11.....	69
Figure 4-26 Ac response of structure 16.....	69
Figure 5-1 Omron D6T-44L [38].....	72
Figure 5-2 Field of view divided into 4-by-4 pixels [38].....	72
Figure 5-3 Difference between pyroelectric and Moron senor.....	73
Figure 5-4 Functional block diagram of sensor interfacing [39].....	74
Figure 5-5 IR sensors' output in 12x4 pixel.....	74
Figure 5-6 IR intensity Vs time for 16 pixels.....	75
Figure 5-7 Tekscan's Flexiforce Sensor	76
Figure 5-8 Interfacing schematic for a sensor	77
Figure 5-9 Schematic diagram of sensor interfacing board	78
Figure 5-10 (a) Inside the case (b) After enclose everything inside.....	79
Figure 5-11 Sensor placed on youBot	79
Figure 5-12 System diagram of real-time hardware	80
Figure 5-13 Snippet of the code	80
Figure 5-14 Block diagram of the software framework.....	81
Figure 5-15 Time test path for youBot.....	83
Figure 5-16 youBot Cartesian position during manikin control	85
Figure 5-17 youBot Cartesian position during tablet control	85
Figure 5-18 (a) Power supply board (b) Data acquisition board.....	87

Figure 5-19 RoboLimb [68] 87

Figure 5-20 A subject (a) Carrying a heavy box (b) Picking up a water bottle 88

List of Tables

Table 3-1 Composition of inks	30
Table 3-2 Parameters for printing (PEDOT:PSS)DMSO ink.....	32
Table 3-3 Parameters for printing (PEDOT:PSS)NMP ink.....	32
Table 3-4 Gage factors for various materials	42
Table 4-1 Temperature Sensitivity	57
Table 4-2 Temperature Sensitivity	59
Table 4-3 Minimum Contact Pressure.....	60
Table 4-4 Sensor Repeatability	62
Table 4-5 SNR of sensor.....	63
Table 4-6 Crosstalk between sensors.....	67
Table 5-1 Task completion times in 20 youBot experiments	84

Chapter 1

Introduction

1.1 Motivation

The word ‘Robot’ was first introduced in a 1921 play R.U.R. by Karel Čapek, to denote fictional automata; more precisely artificial people that we know these days as Humanoid Robot. Their intended goal was to help human beings. Now after almost a century later we have many different kinds of automatons that fall under the title ‘Robot’, which might not even have the same structural shape that was described in the play, but they indeed are being used to facilitate human tasks.

Until about two decades ago, robots were only considered as tools for manufacturing industry [1]. They could reliably perform repeated jobs with predefined trajectories set in a structured environment. Recently, collaborative robots (co-Robots) are trying to make their way into less structured environments and work alongside humans in homes, schools, workplaces, and even in hospitals.

Although present technology allows robots to achieve high levels of accuracy, precision and repeatability of movement well beyond human capabilities, they are less capable than humans in household tasks, for instance to fetch a glass of wine or to take care of a patient [2]. One of the reasons is dynamic structure of the environment that the robots cannot perceive to the extent that a human can. Future coRobots must learn autonomously and adapt with the dynamic environment for safe interaction. Numerous researchers have studied human-robot and robot-environment interaction using vision sensors. However, the perception of contact

interaction between robot and environment also has a significant role during Physical Human Robot Interaction (pHRI).

Haptic communication is one of the ways that humans communicate with each other via the sense of touch. A group from University of Umeå disabled the sense of touch by anesthetizing the skin of the hands to reveal the inconveniences of maintaining the grasp of an object [5]. That is due to the fact that the sense of touch provides us the object's properties such as size, shape, temperature, etc. and raise awareness about the object or environment which in turn helps us to separate what is "me" and what is "not me" [1]. So in order to share the workspace and establish an intuitive physical interaction, coRobots must be endowed with realistic touch sensing capabilities.

For the last 30 years, researchers have been studying skins for robots similar to human beings that can sense temperature and pressure. It has been reported that the robot's ability to detect exterior forces can improve communication with humans and the environment, increase the safety and facilitate the human guided behavior learning [3][4]. This research will one day lead to a robust and dependable human-robot interaction that is adaptable to both different users and tasks. It will expedite the research on social robotics, pHRI and can make Karel Čapek's idea real.

1.2 Challenges

Like human skin, robot skin can have various sensing modalities e.g. pressure, temperature, vibration, proximity etc. Integrating different types of sensors is difficult for conventional semiconductor manufacturing process because of different sensor materials, different process parameters they require, and the 3D

topographical nature of skin. In addition, conventional semiconductor manufacturing has limitations with production on large, uneven and flexible substrates. Flexible substrates are needed because the robot itself has numerous curved shapes.

3D printing is an additive manufacturing technique that has been proposed to manufacture robotic skin sensors. In prior work [70], one such prototype 3D printer consisted of a XYZ stage system with 10um resolution. G-code was used to control the printing procedure resulting in a tedious and slow process to set up and calibrate the sample using manual alignment for every printing task. There are numerous challenges associated with programming and automated calibration of such systems.

Furthermore, the spatial resolution of the sensors needs to be high enough for humans to interact safely. However, data acquisition rates will be affected (slowed) considerably by increasing spatial resolution. Fabrication challenges, including signal routing and packaging also increase as we attempt to miniaturize skin sensors. Thus, developing sensor fabrication and data acquisition methods that are scalable and can be applied to an appropriate pHRI scenario are important challenges to overcome.

Once sensor skin fabrication and interfacing is completed, sensor performance must also be evaluated. Performance includes sensor response to temperature changes, asking questions such as does the output response drift over time etc. Challenges include developing efficient, controlled and automated methodologies to characterize these sensors.

Finally, the sensor performance must be evaluated in conjunction with the robot's control system. For instance, experiments must be conducted to characterize how pressure-sensing capabilities are helping coRobots during pHRI. Is it making any

differences when it comes to human-robot interaction? Challenges include signal filtering, compression, and real-time control during interaction.

1.3 Contributions of this thesis

The work detailed in this thesis covers several aspects of robot skin manufacturing, characterization and application to coRobots. The research contributions of this thesis are:

a. Printing Parameter Optimization

- Electro-Hydro-Dynamic (EHD) printing technology was used to 3D print pressure sensors on flexible substrates. Poly(3,4-ethylenedioxythiophene) polystyrene sulfonate (PEDOT:PSS) piezoresistive material based inks were used to print sensors. The EHD printing procedures and quality both depend on several parameters, such as applied voltage, applied pressure, nozzle distance from substrate, speed of printing etc. Different combination of the parameters were used to print and then compared under the microscope to check the quality of printing in terms of how evenly the ink spreads. This helped us to optimize the printing process. To ease the process and have higher throughput, LabVIEW was used to implement the automation of printing and calibration, replacing previous manual steps.

b. Printed Sensor Characterization

- Once the sensors are ready, those need to go through a set of experiments for characterization and calibration. We worked

with an automated force controlled setup to characterize 4x4 pressure sensor arrays. In addition, we also investigated the sensor response with respect to temperature and humidity changes. Test data was acquired for ten single structure sensors and three 4x4 sensor arrays.

1.4 Thesis Organization

Chapter 2 provides information about background and literature survey on robot skins and sensor fabrication methods. In Chapter 3 the sensor manufacturing procedures is explained along with interfacing with electronics. In Chapter 4, a rigorous sensor testing methodology was proposed with results of our sensors. Chapter 5 describes some of the application on robots that used the pressure sensing capability. Finally, Chapter 6 provides a conclusion and some of the tentative future work.

1.5 List of Publications

1.5.1 Conference Papers

- a. Yetkin, O., Sanford, J., Mirza, F., Karulkar, R., Das, S.K. and Popa, D.O., 2015. Control of a Powered Prosthetic Hand Via a Tracked Glove. *Journal of Medical Devices*, 9(2), p.020920.
- b. Alonso, R., Cremer, S., Mirza, F., Gowda, S., Mastromoro, L. and Popa, D.O., "Multi-modal sensor and HMI integration with applications in personal robotics", *SPIE Sensing Technology+ Applications* (pp. 949409-949409). International Society for Optics and Photonics, June, 2015.

- c. Cremer, S.; Mirza, F.; Popa, D.O., "Investigation of Human-Robot Interface Performance in Household Environments", SPIE, April, 2016.
- d. Mirza, F., Sahasrabuddhe, R.R., Baptist, R.R., Wijesundara, M.B.J., LEE, W.H. and Popa, D.O., 2016, April. Piezoresistive Pressure Sensor Array for Robotic Skin. In *SPIE Defense + Commercial Sensing*. International Society for Optics and Photonics.

Chapter 2

Background and Literature Survey

2.1 Characteristics of Human Skin

CoRobots are required to co-exist in the same workspace as humans for various tasks that requires a dyad effort. In these situations, physical human-robot interaction is inevitable and robots need to perceive human intent. This can be done by developing advance and intuitive interaction capabilities for robots that in turn increase their safety [43][44] and make them adaptable to unstructured and highly dynamic environments. As a result, it is certain coRobots require human like sensory capabilities.

Human skin is multilayered, viscoelastic and non-homogeneous [1]. It consists of multi-modal sensing mechanisms including temperature, vibration, touch and pressure. These sensing capabilities are distributed all over the body with various density. For example, Mechanoreceptors, cells that respond to mechanical stimuli, has a density of $58/\text{cm}^2$ in the palms but has a density of $241/\text{cm}^2$ in fingertips [45]. This density depends on the spatial difference. For instance, in fingers the discrimination acuity between two points is 1mm whereas in forearm it is around 30mm [46]. Furthermore, sensing thresholds are different between men and women: pressure sensitivity thresholds are 3mg and 2.5mg respectively and temperature thresholds are 32°C and 38°C respectively [47].

R. S. Dahiya et al. provides suggestions about robot skin modeled after human skin in [1]. Like human skin, robot skin must be multi-modal, along with different

resolutions depending on location on the robot. Furthermore, the paper infers that the skin surfaces that are exposed to the environment more frequently should require higher sensor density, fast response and high sensitivity.

However, covering the whole robot with skin can reduce data acquisition rates and make the robot and skin a slow response system due to limitations in total processing capability of the system. Taking the analogy with the human body, signals received by the mechanoreceptors are transferred to the central nervous system through nerves in the form of ‘action potentials’, which we can compare with the digital to analog converter [1][48]. These signals go through some preprocessing before passing through the different paths of the body to reduce the load of the central nervous system [1]. A similar idea can be used to design whole body robot skin to handle a large area.

2.2 Research on Robot Skin

If a robot wants to work side by side with a human being, it needs to have the same capabilities that a human has. Human body is covered with skin that helps them to perceive the dynamic structure of the environment with different kinds of sensibilities through the skin.

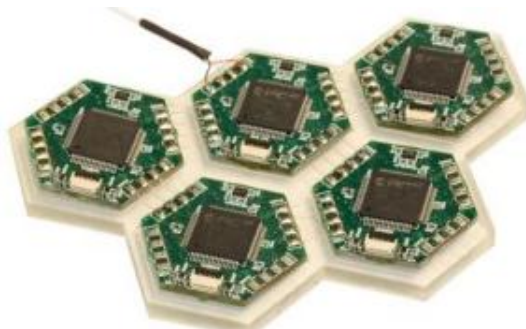
Skin for robots have been studied for several decades and must have similar features in order to interact with human environments [49]. Among all the sensing capabilities, tactile sensing is one of the essential parts as it has been widely reviewed in [50]. As early as 2001, Lumelsky et al. showed how robots could be benefited with IR sensors to interact with humans in an unstructured environment [51]. Much of the

supporting technology, such as manufacturing of flexible PCB or robots with multi-sensing modules have appeared since this pioneering work.

Lumelsky et. al demonstrated a ballerina danced with a sensorized robot arm without colliding with it, which can detect nearby object or humans by using infrared sensing taxels [51]. A leading research group from Germany developed HEX-O-SKIN, a self-organizing multimodal sensing modules that can sense temperature, pressure, acceleration and force [52]. They developed their own pressure sensor while integrating other off-the-shelf sensors into modules. Each module has a unique ID and local intelligence to preprocess information, which in turn reduces the message overhead through the network. An accelerometer maps the modules relative position with respect to the robot host, while each module has four ports to communicate with neighboring modules. A highly redundant sensor structure was demonstrated on a KUKA arm and HRP-2 robot.



(a)



(b)

Figure 2-1 (a) Ballerina dancing with arm [51] (b) HEX-O-SKIN [52]

Another team from Italy developed Roboskin [53], which consists of twelve capacitive pressure sensing taxels, among which two of them are used to compensate

temperature drifting for other ten taxels. They are situated on a flexible triangular shape PCB so that it can be placed on any part of a robot. The module also contains an off-the-shelf analog-to-digital converter and overall thirteen of these modules are connected with each other by I2C bus. The skin was tested on iCub, Kasper and Nao robots.

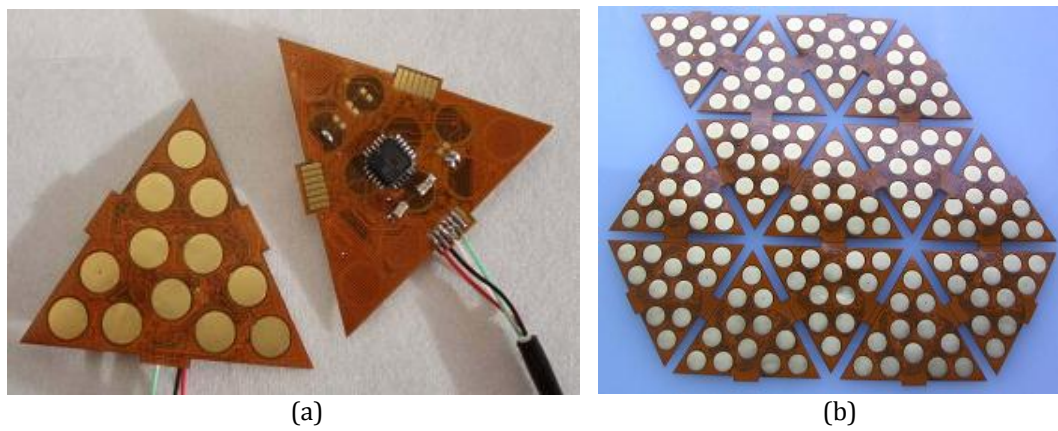


Figure 2-2 (a) Roboskin front and back view [53] (b) Roboskin patch [53]

TakkTile, based on mems barometers, is a low cost tactile sensor that has all the necessary circuitry on a small PCB with a sensitivity of 1 gram [54]. It has a built-in ADC and can communicate with I2C. The PCB is cast under rubber that enhances the sensitivity and consistency. They are available for purchase as either a single sensor or a strip of sensors. They are being used on several dexterous robotic manipulators including the Barrett Arm [55].

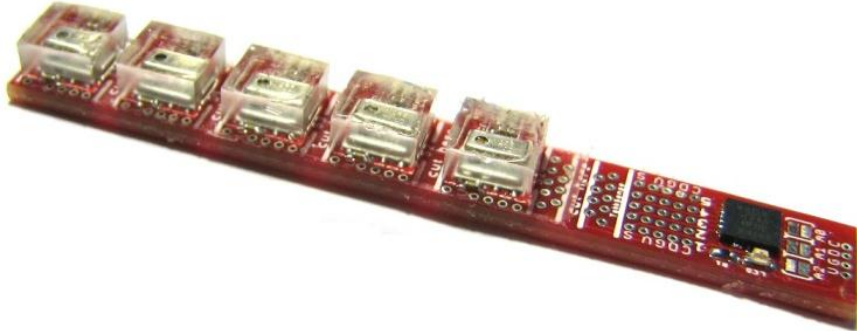


Figure 2-3 Strip of TakkTile pressure sensor [55]

2.3 Robot Skin Sensor Manufacturing Technology

Much of the present semiconductor integrated circuit technology use rigid substrates, such as silicon wafers that are not suitable for robot skin. Robot skin requires sensors on a flexible substrate that can be folded to adapt to various shapes on robot links. Research has been recently conducted towards sensor fabrication on flexible substrates. A group from Princeton University developed elastomeric skin where sub-circuits are interconnected by stretchable metallization [56] on a flexible substrate. Dahiya et al. developed ultra-thin bendable electronic skin that uses $2.5\mu\text{m}$ silicon wires and microstructures on polyimide [57]. Piezoelectric tactile sensors on a flexible ultra-thin polyimide was developed in [57].

Among fabrication techniques, lithography has been widely used to fabricate microelectronics and micro-electro-mechanical systems (MEMS). However, lithography is inherently a batch process with limitations in throughput and time constraints [58]. Furthermore, it is not suitable for structures that have more than two dimensions [59]. As a result, recently some researchers have proposed using 3D printing technology for microstructures [59]. Among non-lithographic methods

Electro-Hydro-Dynamic (EHD) ink-jet printing has the potential features for multi-modal sensors with tunable resolution down to 1 micron. EHD is a non-contact, maskless technique that has high-speed processing and high printing resolution [60].

Chapter 3

Manufacturing of Pressure Sensors for Robot Skins

Physical human-robot interaction requires multi-modal sensors, in a form of artificial skin, especially in a dynamically changing environment. It is challenging to integrate multi-modal sensors under one substrate in standard semiconductor manufacturing methods because of 3-D topographies. Electro-Hydro-Dynamic (EHD) is one of the promising additive manufacturing methods that can be used as an alternative. EHD not only prints micron-sized features with a wide range of ink materials, but can also manufacture large area, and 3D substrates.

In this work, a well-known piezoresistive material, Poly(3,4-ethylenedioxythiophene) polystyrene sulfonate or in short PEDOT:PSS, was used as a pressure sensing material. It is a mixture of two ionomers. Sulfonated polystyrene that carries negative charge and Poly(3,4-ethylenedioxythiophene) that carries the positive charge were mixed together. In this chapter, we describe the implementation of printing station calibration and automation of printing procedures. Furthermore, to test resulting pressure sensor arrays, a data acquisition system was designed using both off-the-self equipment and custom-made hardware. A test matrix was designed for characterization and modelling. The whole process contains several steps from sensor microfabrication to testing as show in Fig. 3-1.

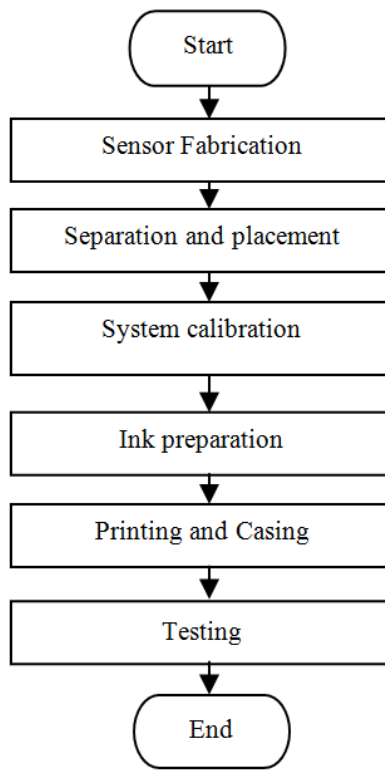


Figure 3-1 Sensor manufacturing steps

3.1 EHD as Printing Technology for Pressure Sensor Arrays

3.1.1 EHD Inkjet Printing

The EHD printing method creates an electric field to dispense fluid out of a nozzle. A high voltage electric field generates well-proportioned jetting, which in turn helps to shrink the smallest features by an order of magnitude below the nozzle size [14]. The nozzle connects to an ink chamber. When pressure is applied to the ink chamber, fluid meniscus forms at the nozzle tip. The high voltage electric field is then applied between the nozzle tip and the ground connected with the substrate. The combination of pressure and electric field jets the ink onto the substrate.

Fig. 3-2 shows the experimental setup for EHD printing in our lab. EHD printing supports a wide range of materials. It can also print high viscosity materials e.g. up to 1000cP, as opposed to 50cP usually achievable with conventional piezoelectric printing.

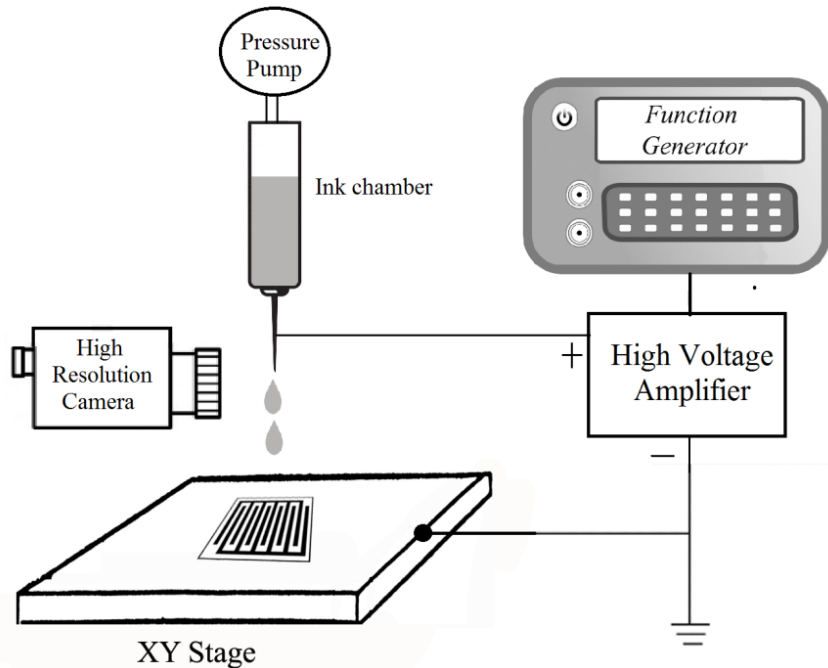


Figure 3-2 EHD Printing Setup

Because of the electric field's pulling and focusing feature, this method can provide finer jetting compared to piezo-jet based printing. Furthermore, the electric field generates a stable and continuous flow, which is helpful to print uniform lines over large areas [15-16]. Combining an EHD nozzle with a CNC machine or a robot, any pattern printing is possible.

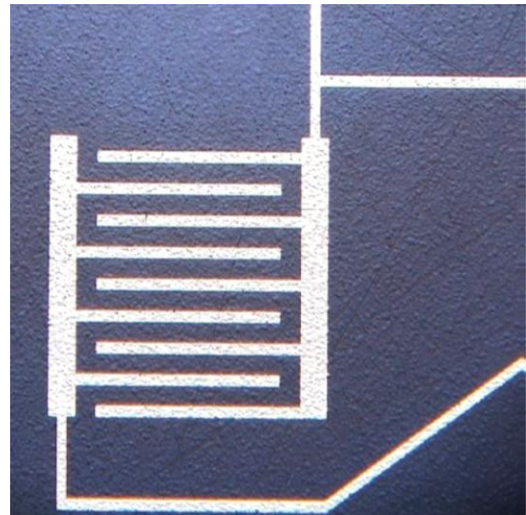
3.1.2 Pressure Sensor

Pressure sensors have been used in industry for numerous applications including biomedical, automobiles, space and environment [17-20]. There are three

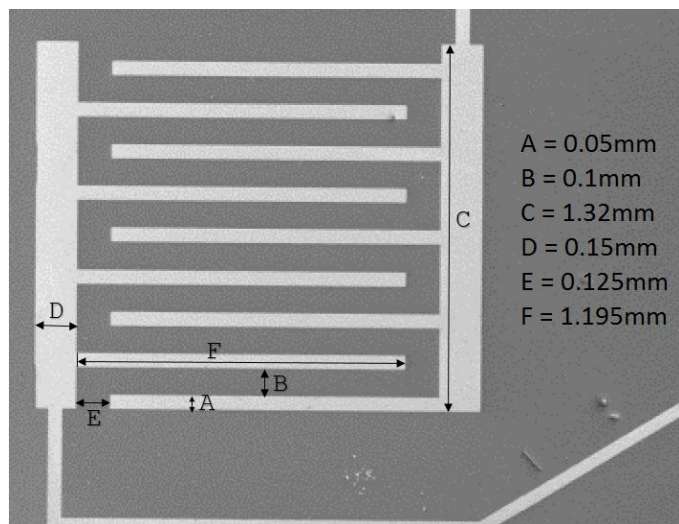
main types of pressure measurement techniques: piezoresistive, piezoelectric and capacitive, and numerous researches have explored these transducers over the years [21-24]. Capacitive sensors create a variable capacitance to detect strain caused by pressure. These sensors are good for low-pressure measurements. However, because of their inherent parasitic noise, their linearization is poor. Piezoelectric sensors are suitable for dynamic pressures but have poor response for measuring static pressures. Piezoresistive sensors provide variable resistance for applied pressure. They are suitable for static and dynamic response, but are generally sensitive to temperature changes. A wide variety of materials exhibit the piezoresistive effect [24-26], with high sensitivity and cost effectiveness in manufacturing.

For this work, we have selected, a piezoresistive sensing material, PEDOT:PSS, to fabricate our pressure sensors. PEDOT:PSS is a conductive and transparent polymer that is stretchable, highly ductile and stable. It has used as smart textiles [27], flexible piezoresistive strain gauge sensors [28][29] and touch sensors [30]. Usually conventional metal films has a gauge factor of 2, PEDOT:PSS's gauge factor ranges from 5 to 20, makes it an ideal choice for our work.

In this work, we have developed a number of PEDOT:PSS inks and fabricated strain sensors for their evaluation. The substrate fabrication is done by microstructuring technology, using lithography, deposition and lift-off to make conductive traces. An interdigitated electrode (IDE) structure with micron-scale features on a flexible polyimide (Kapton) substrate serves as the substrate on which PEDOT inks are printed, as shown in Figure 3-3.



(a)



(b)

Figure 3-3 (a) IDE Structure made of Gold on Kapton Sheet (b) Dimensions (mm)

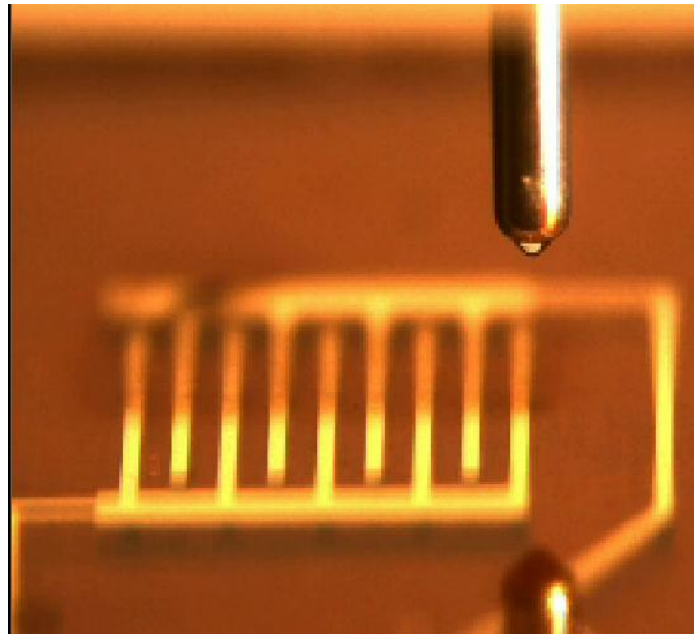


Figure 3-4 Photograph showing the printing nozzle, and ink meniscus above an IDE structure

3.1.3 Ink Formulation

Two different types of inks were formulated using PEDOT:PSS as a primary material. First, high viscosity screen printing PEDOT:PSS paste was dissolved in *N*-Methyl-2-Pyrrolidone(NMP) to obtain desired ink characteristics including low viscosity and low surface tension. NMP was selected due to its low surface tension and high boiling point. A high boiling point allows repeatable printing with no drying of ink in the print nozzle. The weight-to-weight composition of each ink is shown in Table I. Ink 1 contains PEDOT:PSS and NMP. Ink 2 contains PEDOT:PSS and Dimethyl sulfoxide (DMSO). DMSO has a broad collection of miscible organic solvents and has a high melting point.

Table 3-1 Composition of inks

Ink	PEDOT:PSS	Solvent	Solvent Type
1	1	2	NMP
2	1	3	DMSO

The masses of each component of the mixture were measured using an Ohaus model EF214C analytical scale (Fig. 3-5a). The primary solvent is first weighed in a centrifuge tube, along with any other non-colloidal liquids. Solid materials are then added stepwise in ~250mg increments and mixed between each step for 10 seconds with a vortex mixer. In the original vial, the contents are mixed in a rotary tumbler for no less than 5 hours to ensure solids are thoroughly dissolved. After thorough integration of solid materials into the solvent, PEDOT:PSS is added by mass into the solvent mixture. This is done at one time with no intermediate mixing. After the PEDOT:PSS is added, the mixture is re-tumbled for at least 15 hours. Prior to printing, the ink is vortexed then sonicated for 15 minutes.

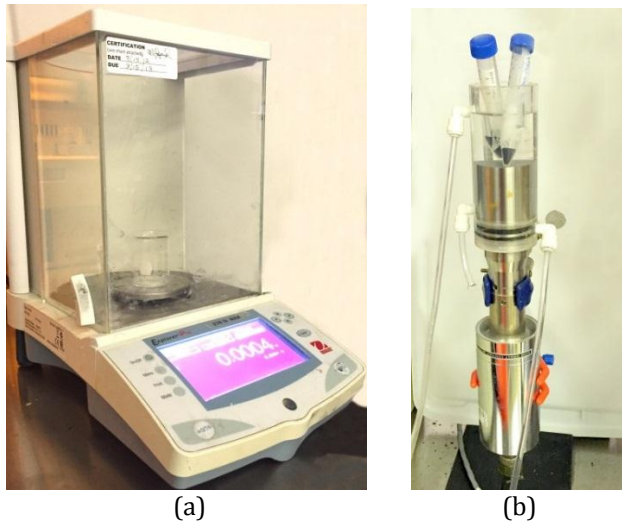


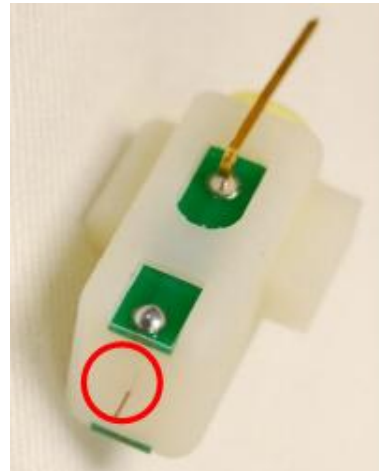
Figure 3-5 (a) Ohaus analytical scale (b) Sonifier

3.1.4 Printing Parameter Optimization

There are four printing parameters that need to be investigated: the applied voltage, pressure, nozzle travel speed and distance between nozzle and substrate. Wide ranges of these parameters were used for a Design of Experiments trial to find optimized parameters for each ink.



(a)



(b)

Figure 3-6 (a) Alicat Pressure Pump (b) 32 Gauge Nozzle

As shown in Figure 3-6 (b), the EHD printer used a 32 gauge nozzle. An Agilent 33220A wave from generator was used to generate 1KHz square wave signals

controlling the electric field in order to obtain drop-on-demand ink jetting. A Trek PM04015A Generator/Amplifier was used as high voltage power supply. For pressure control, the Alicat PCV110 pressure pump shown in Figure 3-6(a) can generate pressures up to 25kPa. Representative parameter optimization trials are shown in Table 2 for DMSO inks and Table 3 for NMP inks.

Table 3-2 Parameters for printing (PEDOT:PSS)DMSO ink

Pressure kPa	Nozzle Spacing	DC voltage V	Speed mm/min
0.15	600	1000	50
0.15	700	1000	150
0.25	600	1600	300
0.50	700	1600	500
1	700	1800	50
1	800	1800	50

Table 3-3 Parameters for printing (PEDOT:PSS)NMP ink

Pressure kPa	Nozzle Spacing	DC voltage V	Speed mm/min
0.15	500	1000	100
0.15	500	1000	150
0.25	600	1200	300
0.25	600	1200	100
0.50	700	1300	50
0.50	700	1400	50

After printing sample sensor lines, these were examined under a Digital Microscope, Hirox KH-7700 shown in figure 3-7, to compare results both quantitatively and qualitatively. Representative printing samples are shown in Figures 3-8 and 3-9.

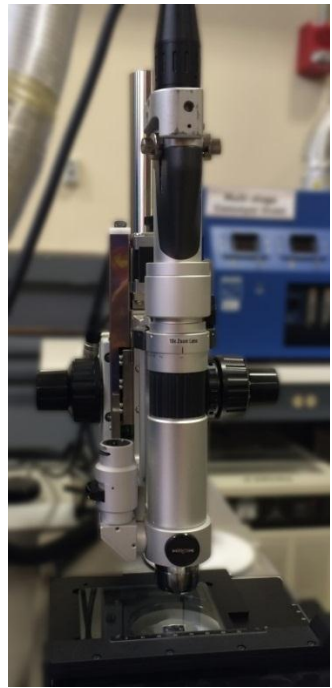
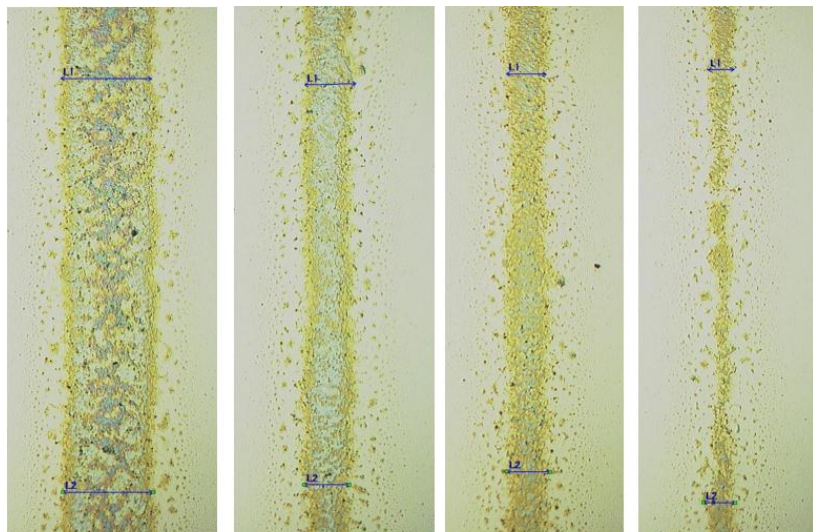


Figure 3-7 Hirox Microscope



LW: ~270 μ m

FR: 50mm/min

~140 μ m

150mm/min

~123 μ m

300mm/min

~185 μ m

500mm/min

Figure 3-8 Sample DMSO ink print with 800 μ m Nozzle Height, 0.9kV, 1kPa

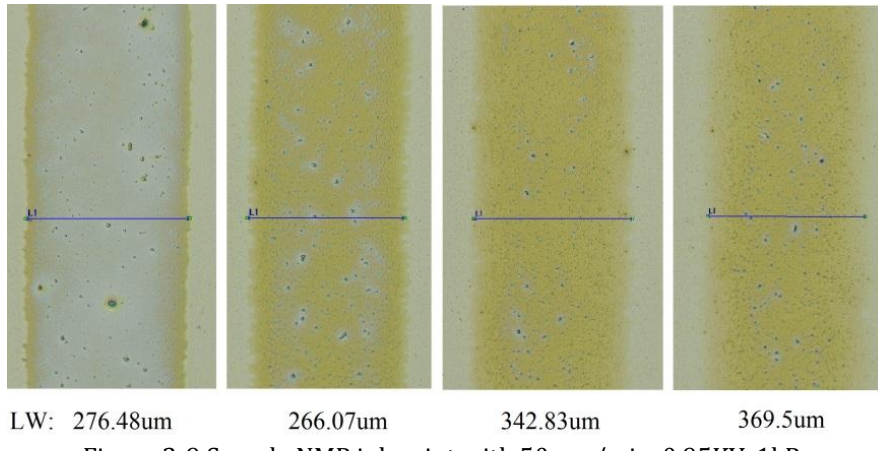


Figure 3-9 Sample NMP ink print with 50mm/min, 0.95KV, 1kPa

3.1.5 Printing Calibration

Characterizing sensors takes a considerable amount of experiments that in turn requires ample numbers of printed sensors. In past work [70], substrates were placed below the print nozzle, and manual alignment of it with the print head axes was necessary. This in turn made the printing process time consuming. In order to speed up, a kinematics identification technique was adapted from [31] in order to map the local coordinate system (sensor's) with respect to a global coordinate system (print head XYZ stage). As a result, the initial orientation of the substrate can be corrected via a few experiments. After this calibration scheme, an open loop controller is good enough to control the stages over large distances (inches) and resulting in large sensor surfaces.

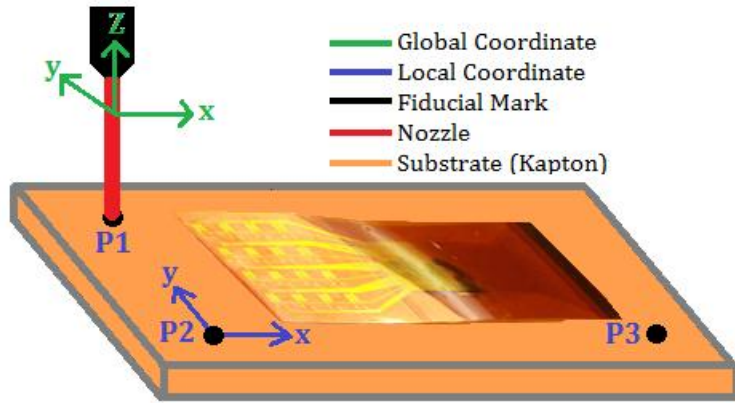


Figure 3-10 Local and Global coordinate frames

The calibration method requires three fiducial marks on the local coordinate system i.e. on the sensor (P_1, P_2, P_3 in Fig. 3-10). The system records those marks in the global coordinate value using encoder values of XYZ stages. After that, global coordinate values to attain a local coordinate point (p, q) can be calculated by equations (3-1) and (3-2) [31].

$$R = R_1 + (R_2 - R_1) \left(\frac{p - p_1}{p_2 - p_1} \right) + (R_3 - \hat{R}) \left(\frac{q - q_1}{q_3 - q_1} \right) \quad (3-1)$$

$$\hat{R} = R_1 + (R_2 - R_1) \left(\frac{p_3 - p_1}{p_2 - p_1} \right) \quad (3-2)$$

$(p_1, q_1), (p_2, q_2), (p_3, q_3)$ are local coordinates of P_1, P_2 and P_3 fiducials respectively (i.e. on the sensor substrate). P is any point of interest on the sensor substrate with local coordinates of (p, q) . R_1, R_2 and R_3 are the global coordinate values of the XYZ stage of P_1, P_2 and P_3 respectively with nozzle pointing to that location, and R represents the global coordinates of the nozzle to point at P .

The values of P_1, P_2 and P_3 can be obtained directly from the design layout, whereas R_1, R_2 and R_3 values are read from the encoder on the print head stages. The

process is observed through a 5x lens CCD camera that provides $3.2\mu\text{m}/\text{pixel}$ image resolution. Figure 3-11 shows a microscope image with several printing via points defined in the local coordinate frame of the substrate.

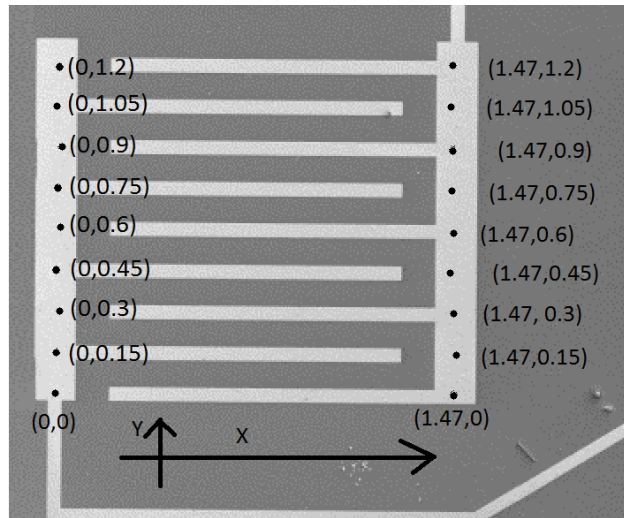


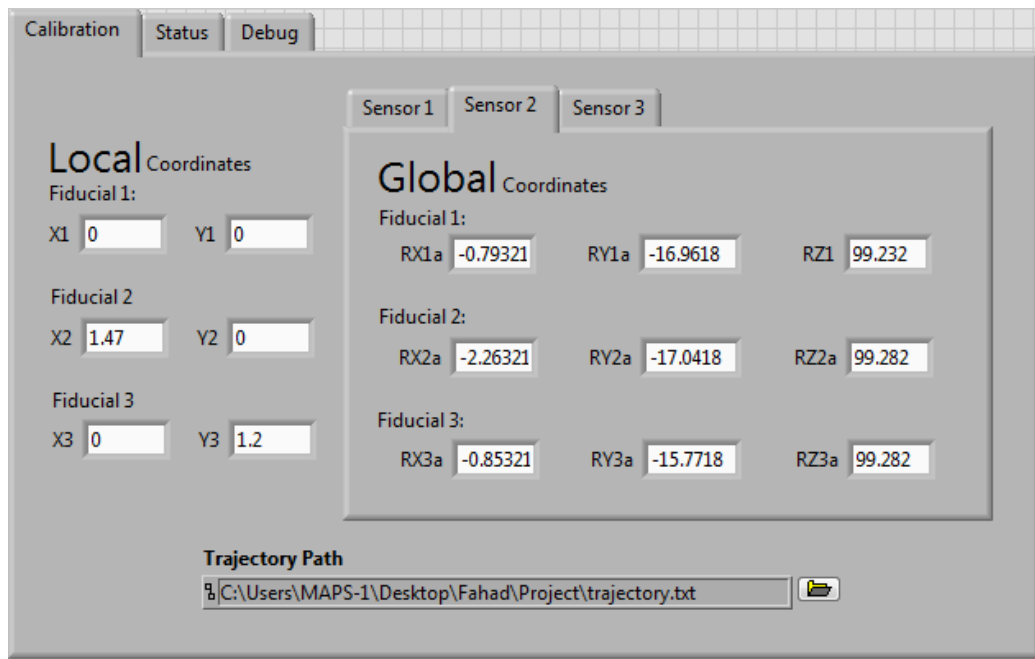
Figure 3-11 Local coordinates (mm)

The XYZ print head positioning system consist of Aerotech stages that are controlled by Aerotech A3200 Direct Drive Stage System (Fig. 3-12). It can control up to 32 axes and supports two communication interfaces, EitherCAT and Profinet. The servo resolution in any axis is as high as $1\mu\text{m}$, adequate for our EHD printing task.

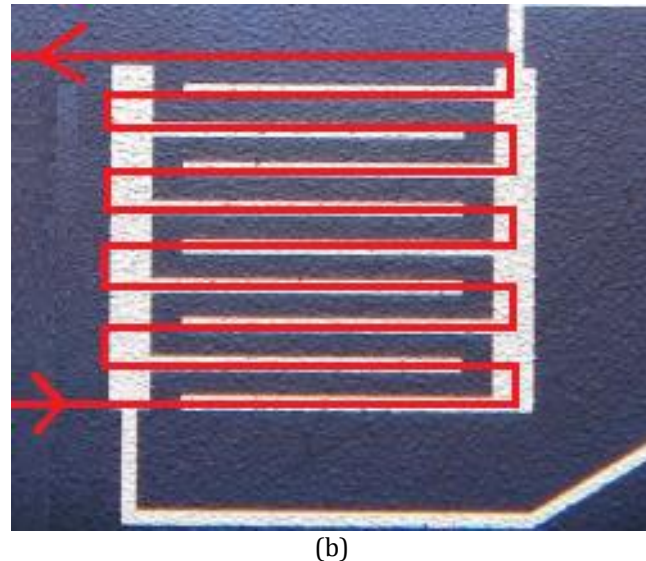


Figure 3-12 Aerotech A3200 System [36]

A program written in LabVIEW was used to program the calibration process and resulting trajectories. After calibration, a user interface accepts fiducial local and global coordinates (Fig. 3-13a) as input. Once the calibration is done, the program loads a set of local coordinates in the form of a text file, and generates XYZ print head position to follow a printing trajectory. A printing path parallel to the direction of the IDE comb was chosen in our experiments (Fig. 3-13b). The program then generates an array of stage encoder values defining trajectory via points. In order to have a continuous motion from one point to another, the distance between two points was calculated and normalized for all the axes and then multiplied that with the desired joint velocity, which was in our case 3mm/s.



(a)



(b)

Figure 3-13 (a) Front panel of the program (b) Printing trajectory

3.2 Printing of Sensor Arrays

Calibration is especially useful when printing larger sensor areas, such as the 4-by-4 sensor array as shown in Fig. 3-14. The tactel sensing area has a dimension of 15.806mm in length and 14.58mm in width. All the single structures have the same dimension as mentioned before and has a spacing of 3.1mm with respect to other structures, both in X and Y direction.

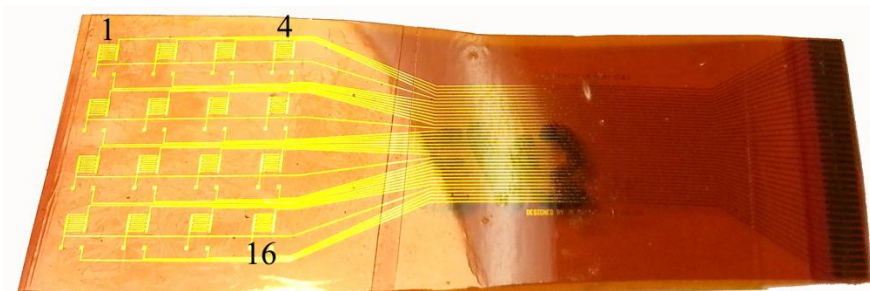


Figure 3-14 Sensor Array showing 16 tactels & corresponding 32 interconnect lines.

3.3 Packaging and Interconnection of Sensors

After EHD printing of PEDOT:PSS based inks onto interdigitated structures, it was necessary to encase the sensor in a material that prevents permeation of moisture or adsorption of other contaminants into the film. In addition, an encasing polymer also acts as an applied force diffusion layer affecting the resulting strain and performance of the sensor. In this work, we used RTV silicone rubbers to enclose the sensor, as depicted in Figure 3-15. They are heat resistant, highly adhesive and have high elongation, high tear strength. In this thesis, we report on testing results with sensor arrays encapsulated in Silicones, Inc.'s P-10 RTV silicone rubber [72]. Other studies have reported on testing results with other skin materials such as Frubber® [70].

At first, the silicone polymer was mixed and degassed. During our experiments it was thoroughly mixed (by weight) in a 10:1 ratio (Polymer base : curing agent), and allowed to degas under vacuum for 15 minutes or until little to no bubbles are visible. The polymer was heat-accelerated cured at 75 °C for 10 minutes. It was then kept at room temperature to cool down before use. Sensor sheets were encased by sandwiched between two polymer pads.

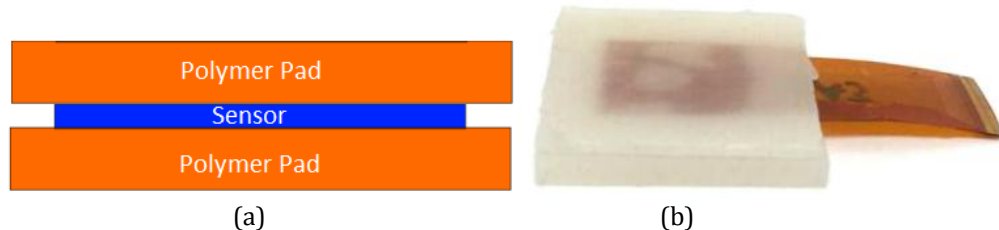


Figure 3-15 (a) Sensor encasing (b) An example of encasing

Electrical interconnection to sensors was obtained through a zero insertion force (ZIF) connector [71]. Single test devices have three ZIF pads, while the arrays have 36 connections. ZIF connectors are simple, cost effective means of connecting ribbon cables to PC boards through an interfacial connection between the contacts inside the connector and the conductive plane on the substrate. This is excellent for quick exchange of sensors and no wire bonding.

A stiffening board is required on the substrate to increase the thickness to nearly 300 microns to ensure sufficient contact to the pins in the connector, and keep it from being pulled out. We put several layers of Kapton tape under the connector portion to thicken it. Connectors have a dimension of 250 x 2500 microns with a 500-micron pitch.



Figure 3-16 Patterned ZIF contact pads. 250x2500 μ m with a 500 μ m pitch

3.4 Interfacing with Electronics

The transduction mechanism for our sensors is based on resistance changing because of strain. In the context of our application the resolution and accuracy needed

to measure resistance changes was beyond the capabilities of regular multimeters. Therefore, special conditioning and amplification circuitry was developed to measure the sensor resistance converted in the form of voltage change.

The diagram in Fig 3-17 shows change in resistance with strain for typical piezoresistive materials. It can be seen that metals such as Rhodium and Platinum show better resistance sensitivity till approximately 0.5% strain. After that they abruptly changes in an undesirable manner. Moreover, Nickel exhibits negative sensitivity for low strain, while other alloy behave comparatively better.

Table 3-4 showcases that the gage factor of such strain sensors is only in the order of unity i.e. changes in resistance in the gage that need to be detected is around 1%. Typically, the strain range that is used in our application is between 2 to 10,000 microstrains [32]. Assume for a material that has 2 GF and 100Ω , which is subjected to strain of 5-microstrain will exhibits approximately 0.001% resistance change. To detect that change, one needs a six digits ohmmeter!

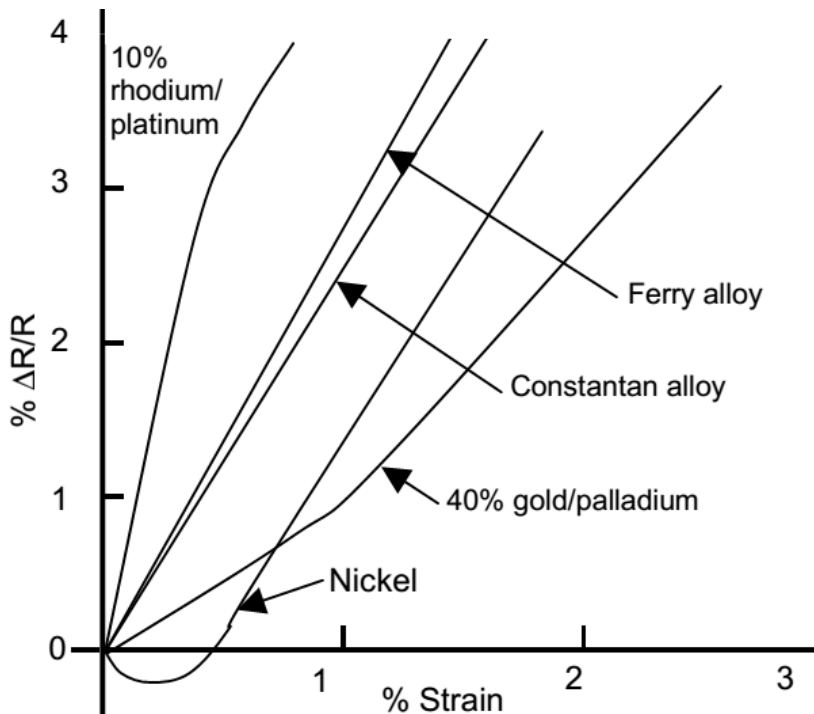


Figure 3-17 Change in resistance with strain for various materials [32]

Table 3-4 Gage factors for various materials [32]

Material	Gage Factor		Elongation (%)
	Low Strain	High Strain	
Constantan	2.1	1.9	1.0
Nickel	-12	2.7	150
Platinum	6.1	2.4	0.4
Palladium	0.9	1.9	0.8
Silver	2.9	2.4	0.8

3.4.1 Wheatstone Bridge

A Wheatstone bridge electrical circuit (Fig 3-18), invented by Samuel Hunter Christie in 1833, is widely known for its accurate measurement capabilities. It has been extensively used to measure resistance, inductance and capacitance [33]. It has been used extensively in strain measurements because of the concept of difference measurement. In Fig 3-18, R_x is unknown, whereas R_1 , R_2 and R_3 are known and R_2 is

adjustable. If the ratio of R_1/R_2 is equal to R_3/R_x then voltage between point B and D will be zero and no current will flow through the galvanometer. This is known as a balanced bridge effect. At the balance point, we can write:

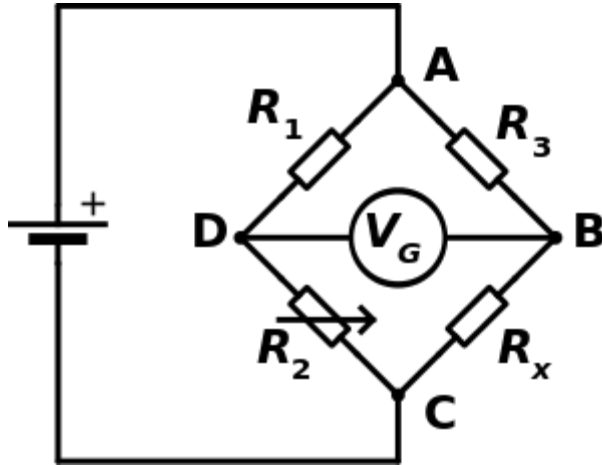


Figure 3-18 Wheatstone bridge circuit [33]

$$\frac{R_1}{R_2} = \frac{R_3}{R_x} \quad \text{or} \quad R_x = \frac{R_3 R_2}{R_1} \quad (3-3)$$

If R_1 , R_2 and R_3 is known to high precision, then R_x can be calculated accurately. A small change in R_x will unbalance the bridge and can be easily detected. Even if R_2 is not adjustable, the voltage across point B and D can be used to calculate the value of R_x . We use this effect to monitor changes in resistance of PEDOT films across our IDE electrodes while straining the substrate.

3.4.2 Instrumentation Amplifier

An instrumentation amplifier is a type of differential amplifier, made out of three operational amplifier (Fig. 3-19) [34]. The leftmost two opamps are buffering inputs and the rightmost opamp serves as impedance matching to a data acquisition

system. Because of its low noise, low drift, low DC offset, low CMMR and high open-loop gain, high input impedance, they are used where high accuracy is desirable. The output of the circuit can be calculated as:

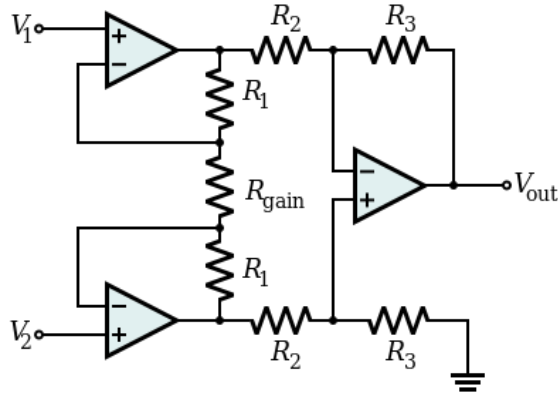


Figure 3-19 Instrumentational Amplifier schematic [34]

$$V_{out} = (V_2 - V_1) \left(1 + \frac{2R_1}{R_{gain}} \right) \frac{R_3}{R_2}$$

(3-4)
Output from Wheatstone bridge's point B and D are connect to V_1 and V_2 .

Although R_2 and R_3 are set by manufacturer, R_{gain} can be set externally, hence, we can control the desired gain of the difference signal. An instrumentation amplifier was used in this work to amplify the Wheatstone bridge signal during straining of our piezoresistive substrate.

3.4.3 Butterworth filter

Butterworth filters are a type of filter that exhibit maximally flat frequency responses (i.e. no ripples) in the passband [35]. Although it provides linear phase in the passband, this is achieved with the tradeoff of slower roll-off towards stopband. Slower rolls can be improved with higher order filters, as shown in Fig. 3-20. A first

order has a roll-off of -20dB per decade, second order has -40dB and so on. It increases with the order of -20ndB, where n is the order of the filter.

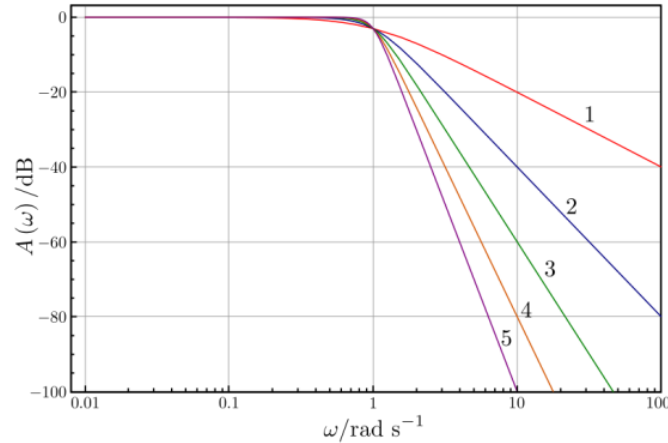


Figure 3-20 Frequency response of BW LP filter from order 1 through 5 [35]

A Butterworth Low-Pass filter's amplitude response is (with unity gain) given by:

$$|H(j\omega)| = \frac{1}{\sqrt{1 + \left(\frac{\omega}{\omega_c}\right)^{2n}}}$$

Where, ω_c is the filter cut-off frequency and n is the filter order. The Sallen-key (3-5) topology (Fig. 3-21) is a well-known suitable configuration for Butterworth filters [37]. It is a second order active filter with a cut-off frequency given by:

$$f_c = \frac{1}{2\pi\sqrt{R_1 R_2 C_1 C_3}}$$

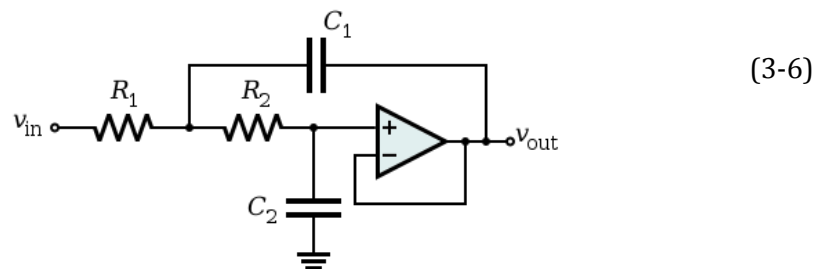


Figure 3-21 Unity gain Butterworth LP filter with Sallen-Key topology [37] (3-8)

In this work, a Butterworth filter circuit was designed and implemented for pressure sensor signal conditioning after amplification.

3.4.4 Single sensor interfacing

An electronic board was designed to interface a single structure IDE sensor by combining the bridge, amplifier and filter previously discussed. $10K\Omega$ was used as R1 and R3 to keep the current flow through the sensor minimal. The resistors have 0.05% tolerance. The resistance of our sensors vary between 100Ω to 400Ω . Therefore, we used a $1K\Omega$ potentiometer as R2. The board also has its own Low-Dropout regulator (LM3480) to regulate a steady power supply for the board along with filtering capacitors for all the ICs power supply pins. The instrumentation amplifier, AD623, is outstanding at measuring small signals over a wide range of temperature. It has ultralow input noise performance of $1nV/\sqrt{Hz}$ along with high Common Mode Rejection Ratio (CMRR). CMRR increases with the increase of gain, which is suitable for our application. The gain can be set from 1 to 1000 using only one resistor. The output of the AD623 is given by:

$$V_{out} = G \times (V_{IN+} - V_{IN-}) + V_{ref}$$

$$G = 1 + \frac{100K\Omega}{R_G}$$

Where G is the gain and can be set by R_G . In our case, we used 200Ω that will give us a gain of 501. To maintain a low source impedance to the REF terminal, a buffer was used with ADA4638 opamp. The PCB was designed to suppress all kinds of EMI noise and is shown in Figure 3-22.

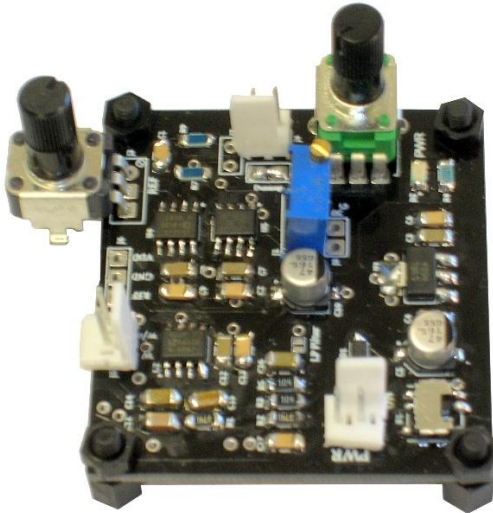


Figure 3-22 Single sensor interfacing board

3.4.5 Sensor Array interfacing - SkinCell

Finally, a sensor array was interfaced to service 16 single interdigitated structures in a 4-by-4 arrangement (Fig. 3-14). It was named SkinCell. Instead of impractically building 16 identical signal conditioners for single sensors, we added an analog multiplexer, CD74HC4067, which can switch between those 16 IDE structures and connect those with the branch (R_x , Fig. 3-18) of the Wheatstone bridge one at a time. Furthermore, as different IDE structures have different resistance value, a digital potentiometer, AD5174, was used in the place of R_2 to balance out the bridge by tuning for individual IDE structure resistances. It is a $10K\Omega$ potentiometer with 1024 position and can be configured by SPI protocol.

The data acquisition system for the entire 4x4 SkinCell was controlled from an IC, ATmega2560. It is an 8-bit RISC based microcontroller manufactured by

ATMEL. It is a high-performance, low power system with 86 general-purpose I/O pins, 4 USARTs and 10-bit A/D converter. It can achieve a throughput of 16 MIPS.

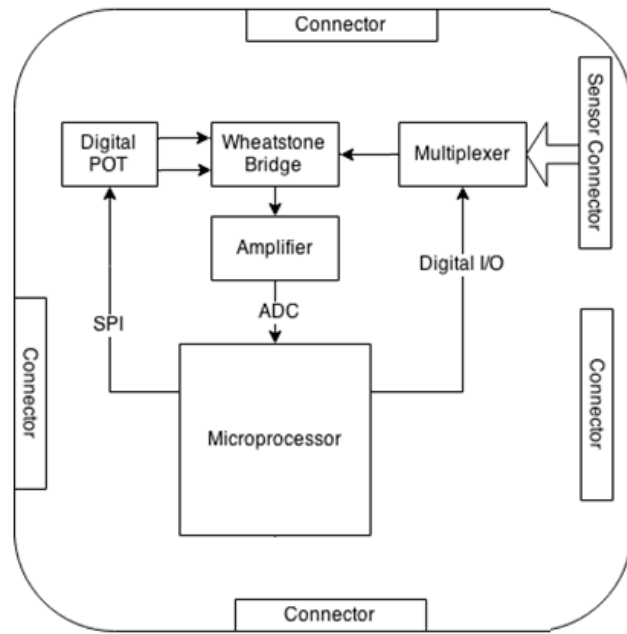


Figure 3-23 Block diagram of SkinCell

The block diagram of the SkinCell is shown in Fig. 3-23. The digital potentiometer was configured through the SPI bus, while the output of the instrumentation amplifier is connected with an ADC channel. In order to provide a scalable design for large area robot skins, the SkinCell was designed to communicate with neighboring SkinCells through USART, which is placed on the four sides of the board. The resulting printed circuit board of a SkinCell has dimension of 48mm by 50mm as shown in Figure 3-24.



Figure 3-24 sensor array connected with the SkinCell

To portray the sensor response, ADC conversion value was relayed back to a computer using USART communication protocol through an USART to USB converter. With ATmega2560 clock cycle set as 16MHz, SPI set as 4Mbps, USART set as 115200bps, and ADC clock cycle set as 125KHz we achieved a 124Hz data rate that provides all 16 IDE structures' response value in a comma-delimited string.

Chapter 4

Experimental Results

In this chapter we described the testing hardware used to evaluate the performance of pressure sensors fabricated using EHD printing. We conducted loading/unloading tests and investigated temperature and humidity sensitivity of sensors, which will be important for the use of these skins for human-robot interaction. Two different sets of setup were used to conduct the experiments.

4.1 Testing Hardware Setup

First setup was used to conduct loading/unloading tests on the sensors. Testing these sensor requires a better set of equipment that has high-resolution analog-to-digital converter, susceptible to noise and can collect data real time. We used National Instruments real-time FPGA hardware, compactRIO (cRIO), controlled by the software package, LabVIEW. cRIO is reconfigurable and deterministic hardware that can programmed by LabVIEW. It has a 400MHz processor and eight slots for swappable devices.



Figure 4-1 NI cRIO-9074 [61]

Two modules were used with cRIO. NI9201, an analog-to-digital converter that has 32 single ended input channel with 12-bit resolution with a range of 0V to 5V and a sampling rate of 500KS/s and a servo motor controller, NI9516, with dual

encoder feedback and position and torque control [62]. ADC module was used to collect sensors' information (our sensor and load cell) and servo module was used to control Newport actuator, which was used to apply pressure on our sensor. A functional block diagram is shown in Figure 4-2 and it was detailed in [70]. As shown in Figures 4-3 and 4-4, a plunger attached to the Newport vertical actuator was used to load the SkinCells under controlled pressure conditions.

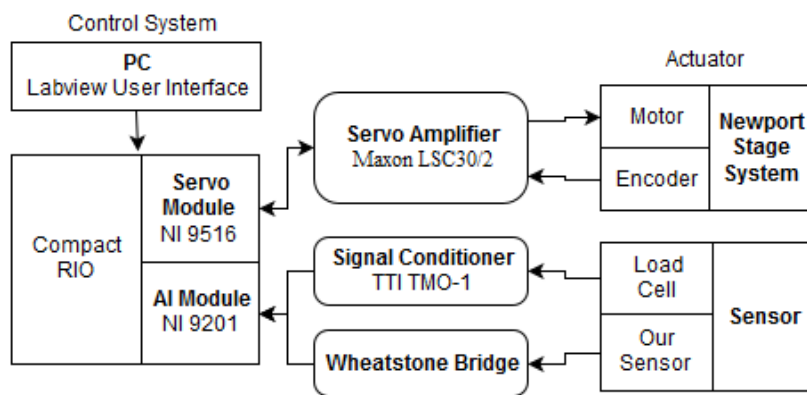


Figure 4-2 Functional block diagram of hardware setup

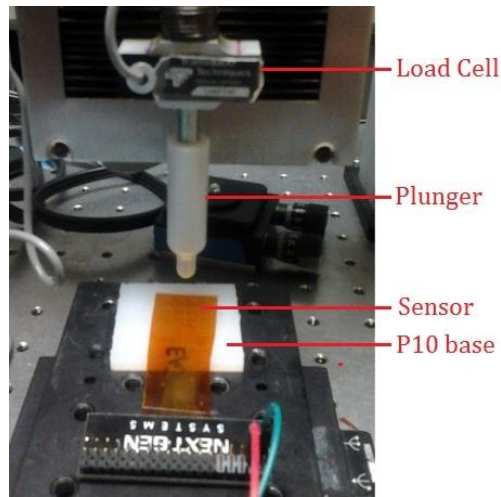


Figure 4-3 Experimental Setup

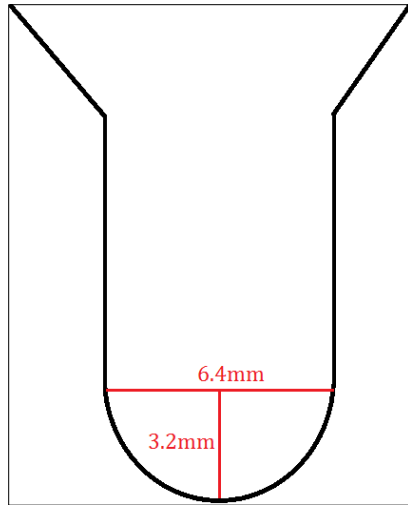


Figure 4-4 Tip Dimension

In the second setup an off-the shelf temperature and humidity sensor, HTU21D, from Measurement Specialties, was used to log the temperature change above pressure sensor substrates. Both the temperature sensor and our sensor array were covered by a cardboard box (Fig. 4-5) and the temperature of the environment was increased by an external heat source and decreased to a lower than room temperature by using dry ice. Although the temperature and pressure sensors locations were not identical, the close proximity and the small volume of the cardbox made it likely that they experienced close temperature variations.

Finally, the same sensor, HTU21D, is used to conduct humidity sensitivity experiment. Humidity of the environment was changed by applying water vapor. Water was boiled to generate humid air and passed to the cardboard box by a fan.

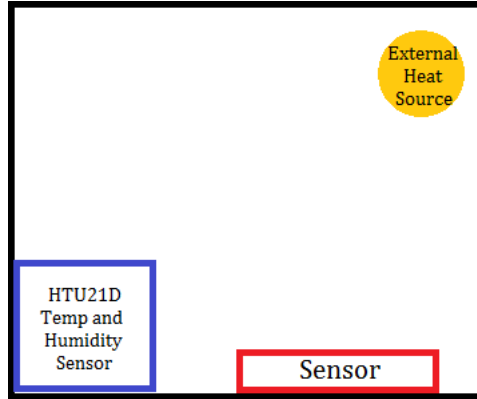


Figure 4-5 Temperature and humidity effect test setup

For this thesis three 4x4 sensor arrays with one layer of PEDOT:PSS(DMSO) ink were used for testing. A 4mm P-10 Silicone Rubber pad was used under the sensors. The sensor and the P-10 pad was placed on an X-Y stage (Fig. 4-6) that was used to adjust the sensor position with respect to the plunger. The stage has two microscales for X and Y axes, respectively, for stage position re-adjustment.

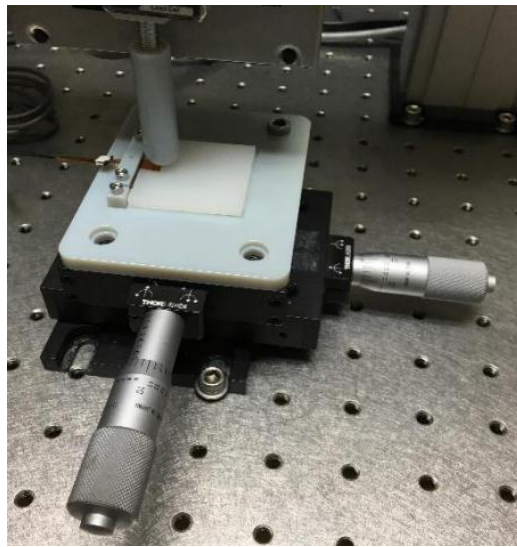


Figure 4-6 Temperature and humidity effect test setup

The plunger was positioned above every IDE structure using this X-Y stage. For most of the tests that required applied pressure were done by applying static pressure i.e. the required pressure was applied and hold on the sensor. One test was done by applying a sinusoidal motion of the plunger. For all the experiments, the bias values (i.e. initial values of the sensors) were subtracted from the sensor responses.

4.2 Experimental Results

4.2.1 Temperature Sensitivity

We conducted temperature-cycling tests for our Skin Cells and individual sensors to investigate their sensitivity. The sensor environment started at room temperature, 24°C , and was heat up to around 40°C and then cooled down to around 10°C and came back to the room temperature again. Fig. 4-7 to 4-11 shows sensor array response with temperature change with respect to time. The average of all 16 structure is shown in red. Black line represents temperature over time.

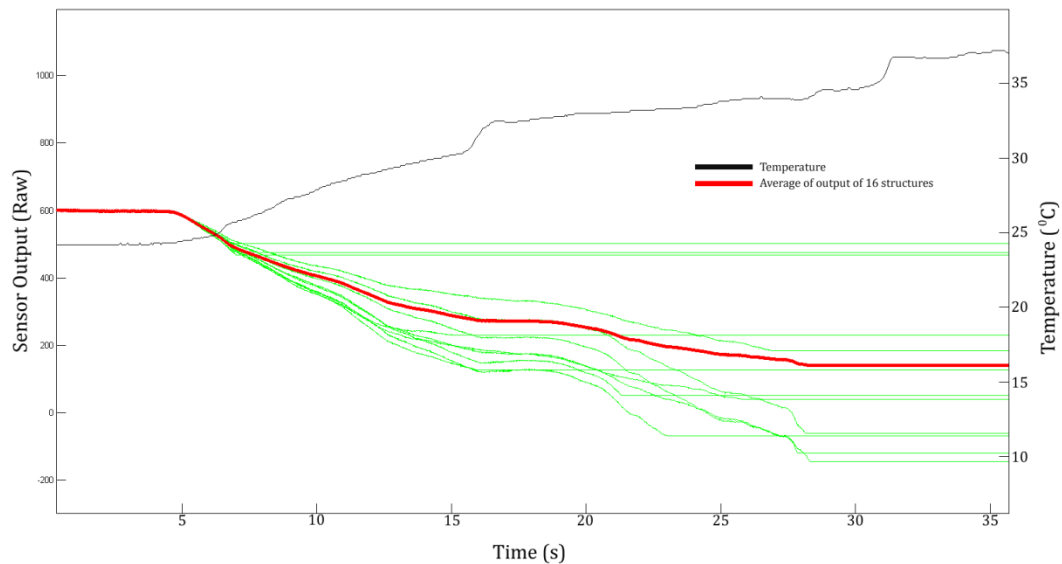


Figure 4-7 Variation of the sensor response with increasing temperature

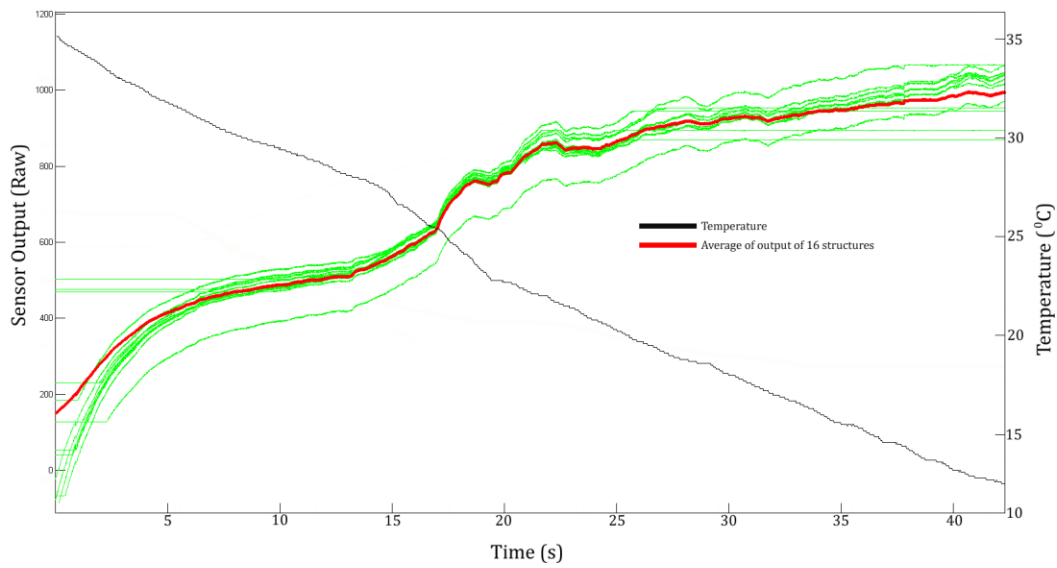


Figure 4-8 Variation of the sensor response with decreasing temperature

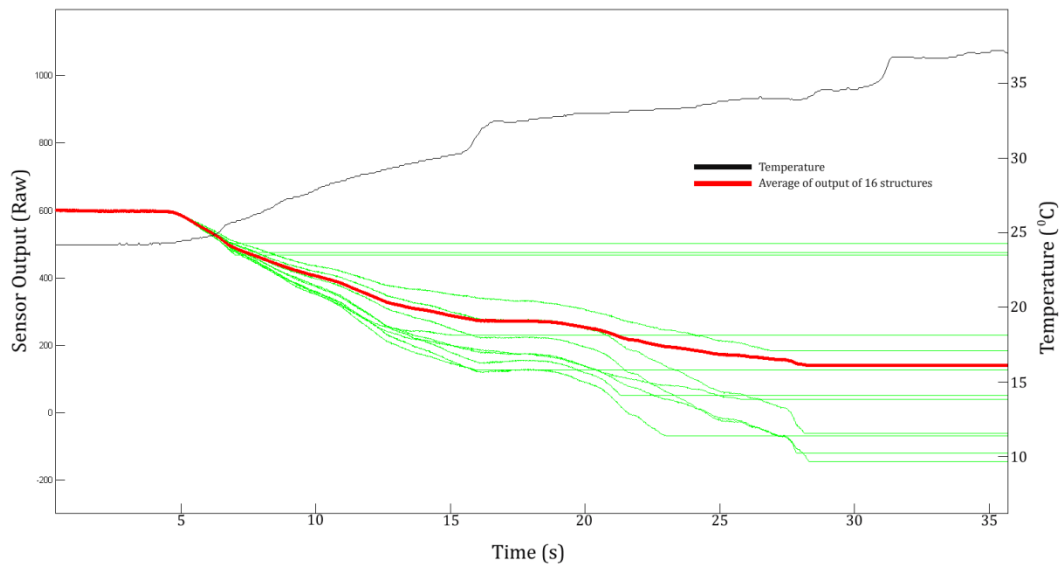


Figure 4-9 Variation of the sensor response with return to room temperature

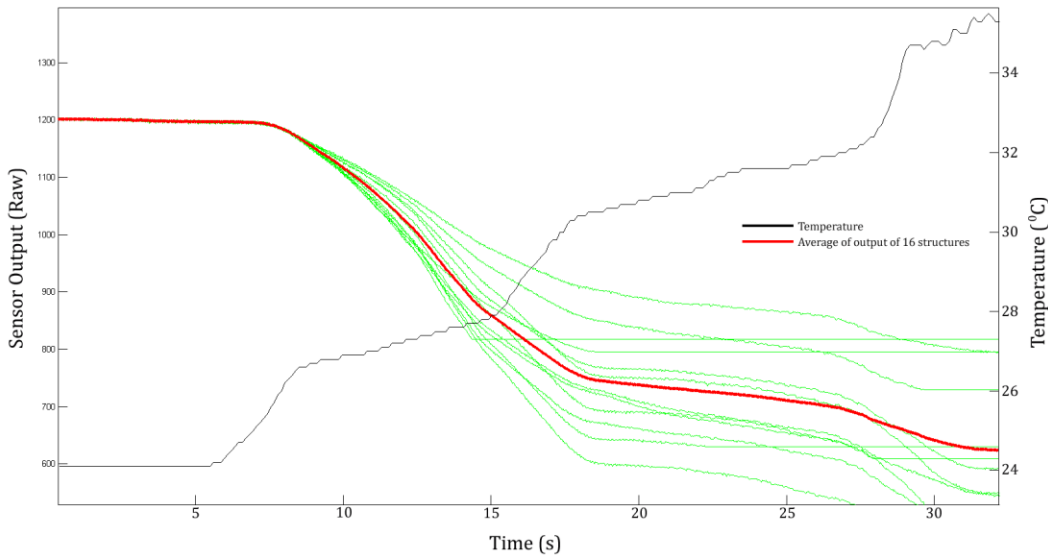


Figure 4-10 Sensor 2 response with increasing temperature.

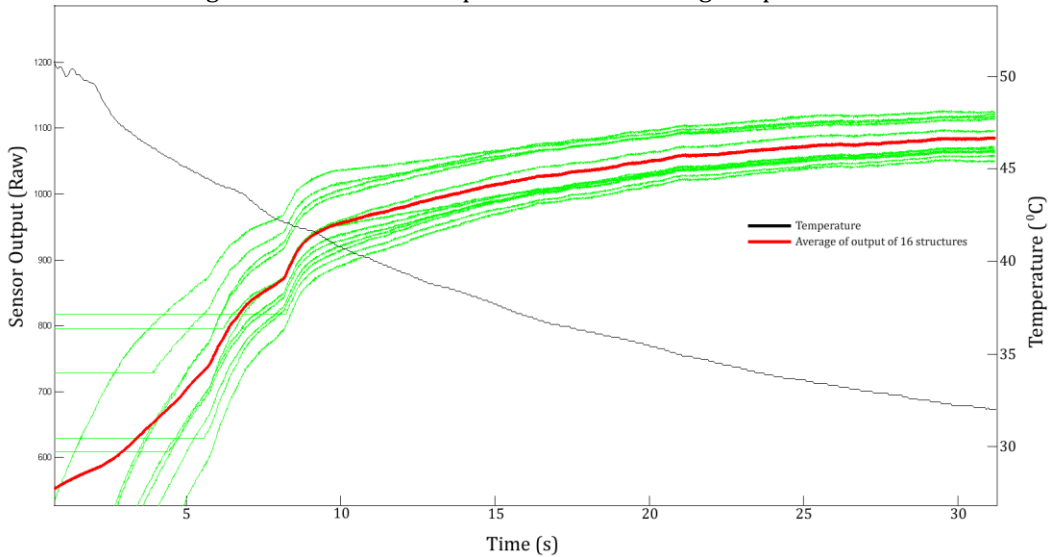


Figure 4-11 Sensor 2 response with return to room temperature

The test was conducted on 28 IDE structures for three times. Fig. 4-12(4.3) shows one example of sensor response vs temperature change. In order to reveal the linear relationships between sensor responses and temperature changes we applied trendlines [73] using:

$$\alpha = \frac{n \sum(xy) - \sum x \sum y}{n \sum x^2 - (\sum x)^2}$$

$$\beta = \frac{\sum y - \alpha \sum x}{n} \dots \dots \dots (4-1)$$

$$T = \alpha x + \beta$$

Where,

n = Number of points

x, y = Corresponding points

α = Slope

β = Offset

T = Trendline

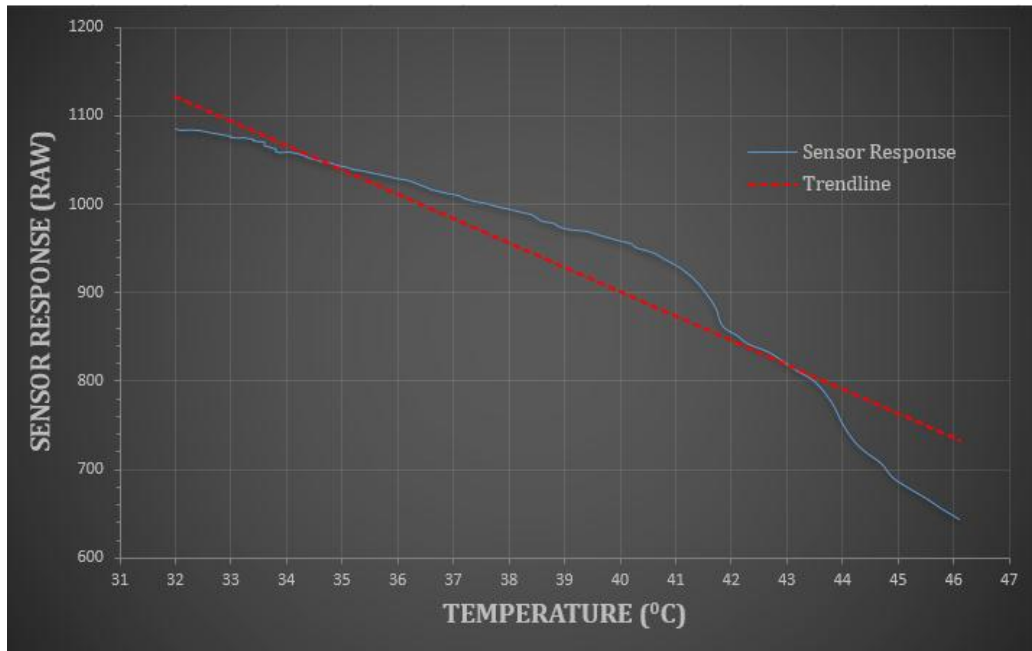


Figure 4-12 Sensor response Vs temperature

Table 4-1 Temperature Sensitivity

Test No.	Resistance in room temperature (Ω)	Sensitivity, α (mV/ $^{\circ}$ C)	Average Sensitivity (mV/ $^{\circ}$ C)
1	345	190	175
2	212	170	

3	250	176
4	301	150
5	313	180
6	225	175
7	311	183
8	330	181
9	280	176
10	202	140
11	323	191
12	295	182

4.2.2 Humidity Sensitivity

Fig. 4-13 and Fig. 4-14 shows the responses of two sensors with respect to humidity changes.

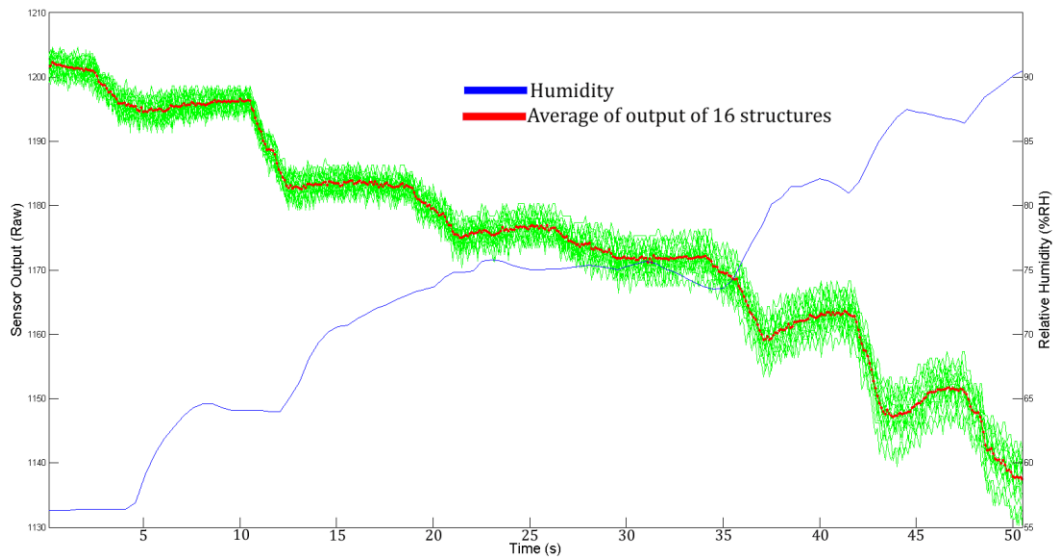


Figure 4-13 Sensor 1 response with change of humidity

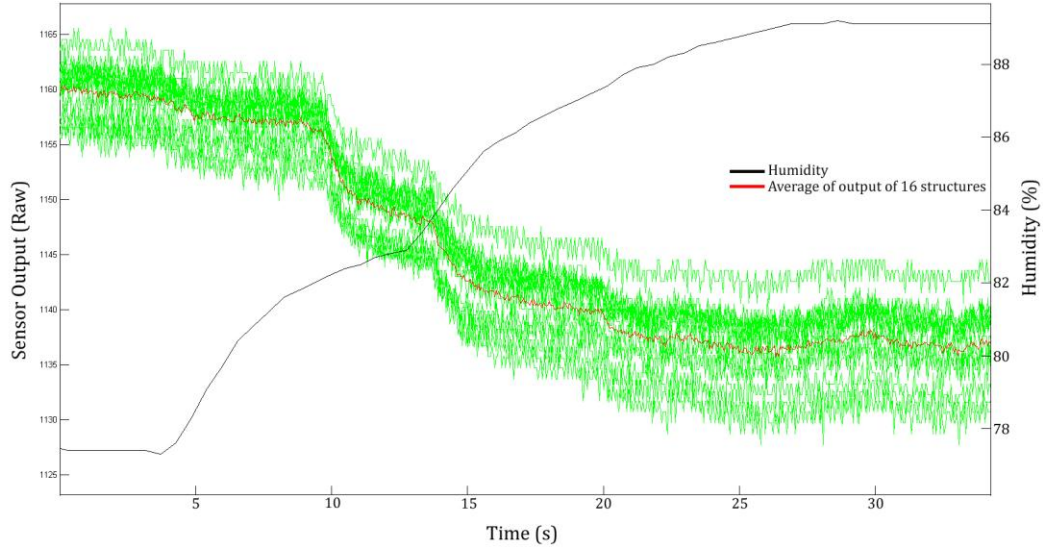


Figure 4-14 Sensor 2 response with change of humidity

Although the humidity and pressure sensors locations were not identical, the close proximity and the small volume of the cardbox made it likely that they experienced close humidity variations. The test was conducted on 28 IDE structures for three times. In order to reveal the linear relationships between sensor responses and temperature changes we applied trendlines.

Table 4-2 Temperature Sensitivity

Test No.	Resistance in room temperature (Ω)	Sensitivity, α (mV/%RH)	Average Sensitivity (mV/%RH)
1	345	8.54	7.88
2	212	7.89	
3	250	7.56	
4	301	8.02	
5	313	8.12	
6	225	7.6	
7	311	8.3	
8	330	8.4	
9	280	7.68	
10	202	6.89	
11	323	7.8	
12	295	7.81	

4.2.3 Contact Pressure

Several sensor arrays were tested by loading and unloading them using the plunger depicted in Figure 4-3. The ADC of ATmega2560 on the SkinCell interfacing board has 10-bit resolution and a range of 0v to 5v. In other word 1-bit represents 4.9mV approximately. We attempted to determine the contact threshold pressure of the sensor by applying pressure to generate at least 2-bits or 10mV (approx.) change at the output. In order to account for interior and boundary effects this experiment was conducted on IDE structures, e.g. tactels 1, 6, 11, and 16 marked in Figure 4-15. As mentioned in the beginning of the chapter P-10 silicone rubber was used under the sensor, but nothing was placed on top of the sensor to avoid additional crosstalk and non-linearity. Furthermore, the sensor and electronics was warmed up by keep the hardware on for 60 minutes to avoid any temporal thermal drift.



Figure 4-15 Sensor array with markings

Experimental results are shown in Table 4-3. The experiment was conducted on three sensor arrays for 5 times each.

Table 4-3 Minimum Contact Pressure

Structure No.	Contact Pressure (lb/in ²)	Avg. (lb/in ²)
1	10.31	11.47
6	11.97	
11	13.63	

16	9.97	
----	------	--

4.2.4 Repeatability

This experiment tested how repeatable sensor response is with a fixed applied pressure. The experiment was conducted on structures 1, 6, 11, and 16 to have both interior and edge effects. 1lb pressure was applied and repeated for 10 times for each target. With each trial, the responses were averaged over time. Between measurements, the plunger was off the sensor. P10 silicone rubber was used under the sensor (Fig-4-3), but nothing was placed on top of the sensor in order to avoid additional non-linearity. The sensor and electronics was warmed up for 60 minutes to avoid any temporal thermal drift. Results are shown in Figure 4-16.

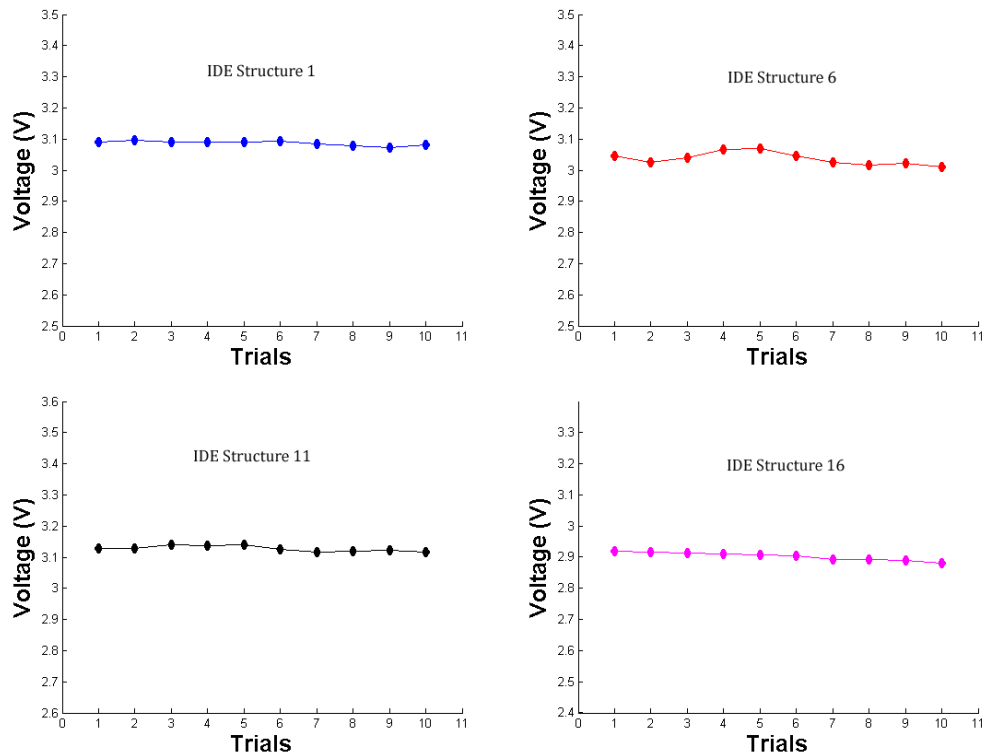


Figure 4-16 Repeatability test results

To analyze this data, we calculated the standard deviation by:

$$r = \sqrt{\frac{1}{N-1} \sum_{i=1}^N (x_i - \bar{x})^2}$$

Where, r = std. dev.

N = number of samples

x_i = ith measurement

\bar{x} = average of all the samples

Table 4-4 depicts the resulting performance of loading the plunger on top of tactels 1, 6, 11, 16 respectively

Table 4-4 Sensor Repeatability

Structure	Avg. Applied Pressure (lb)	Avg. Output (V)	Std. Dev. (mV)	Avg. Std. Dev. (mV)
1	1.0618	3.0864	7.1	12.43
6	1.0434	3.0368	20.7	
11	1.0569	3.1269	12.9	
16	1.0488	2.9023	9.0	

The result shows that loading tactels 1 and 16 have smaller standard deviation than tactels 6 and 11. They being closer to the edge of the sensor, thus experiencing more strain, can explain this. Overall, the sensor exhibits 90% repeatability.

4.2.5 Noise Sensitivity

Noise is an inseparable issue when it comes to real world signals. Signal-to-Noise Ratio (SNR) shows how much a signal is effected by noise. This gives an idea how strong a signal is compared to unwanted noise. It is defined as:

$$SNR = \frac{\mu_P - \mu_R}{\sigma}$$

Where:

μ_P = Mean value when pressure is applied

μ_R = Mean value in resting position

σ = Standard deviation of the signal

An example of SNR calculation is shown in Fig. 4-17 across structure 16. μ_P and μ_R were chosen as a little less and a little more, respectively, to make sure it covers all the averaged values. Standard deviation was calculated from the resting position noise. 1lb pressure was applied and held on it for 10 seconds. In between measurements, the tip was off the sensor. The procedure was repeated 10 times.

Table 4-5 SNR of sensor

Structure	Std. Dev.	SNR
1	1.7844	13.07
6	2.6144	17.01
11	2.02	16.92
16	2.1376	20.6

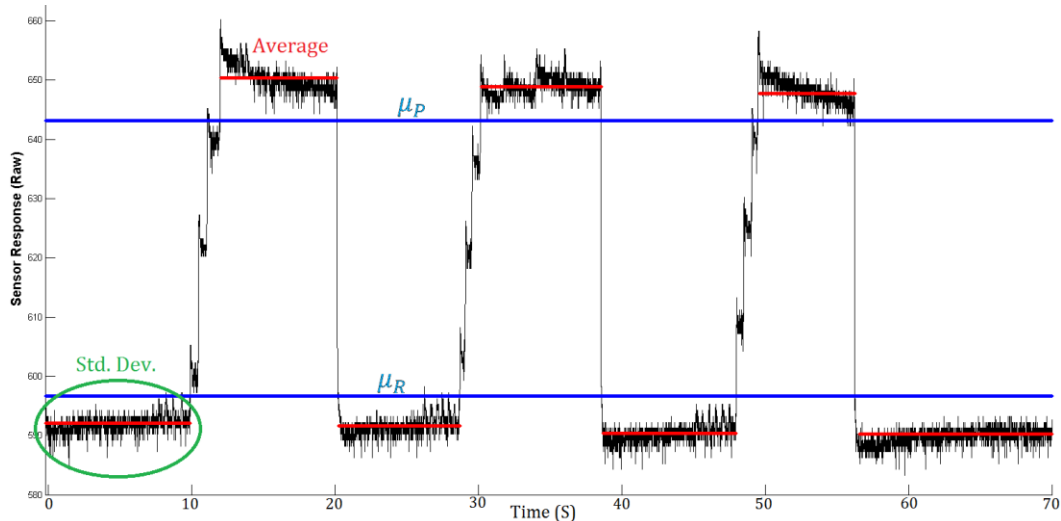


Figure 4-17 Structure 16 SNR calculation

The results shown in Table 4-5 can provide insight into the amount of SNR expected from the sensor array. Structure 1 is the farthest structure from the

connecting pad, hence affected most by the noise while structure 16 is the nearest structure and hence less affected by noise. Being furthest means, a greater length of the conductive trace was open to the environment that attracted the EMI signals. A proper shielding can reduce the noises.

4.2.6 Linearity

Force was applied on the sensor from 0lb to 2lb and the output of the sensor was recorded. The response (Fig. 4-18) is quite linear. Also the result depicts hysteresis effect during loading and unloading.

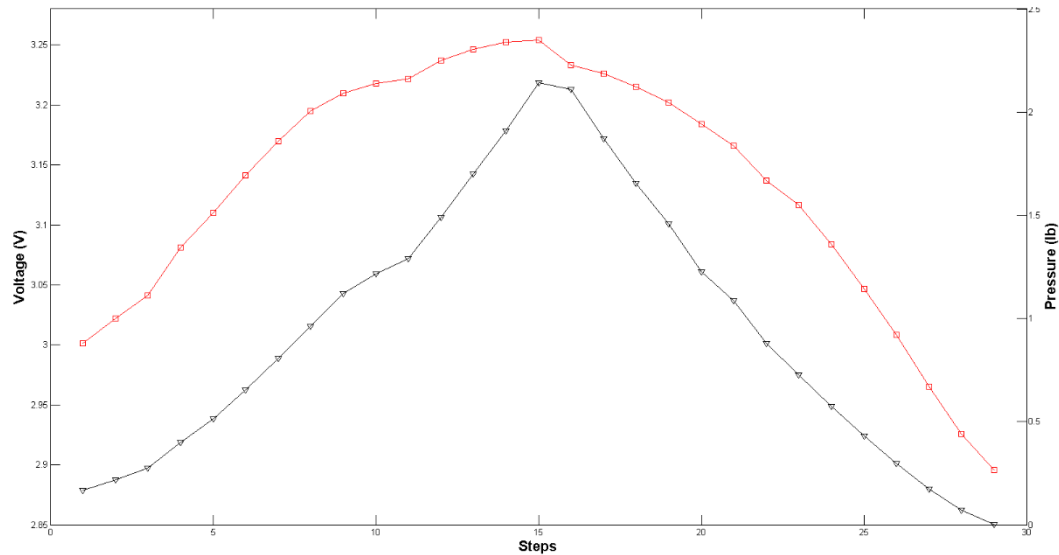


Figure 4-18 Linearity test

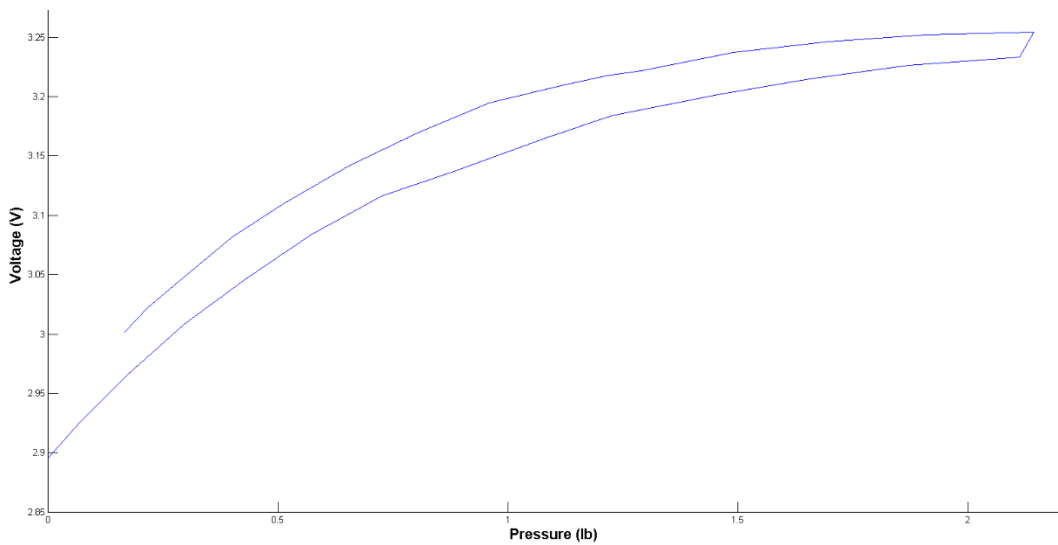


Figure 4-19 Hysteresis effect

4.2.7 Thermal Drift

The sensor was monitored over the period of an hour. There was not any excitation i.e. pressure was not applied during this period. Fig. 4-20 shows the average of all 16 structures of a sensor. The result exhibits that the sensor has positive temperature coefficient i.e. the resistance increases with an increase in temperature. The rate of change is higher at the beginning but decreases over time.

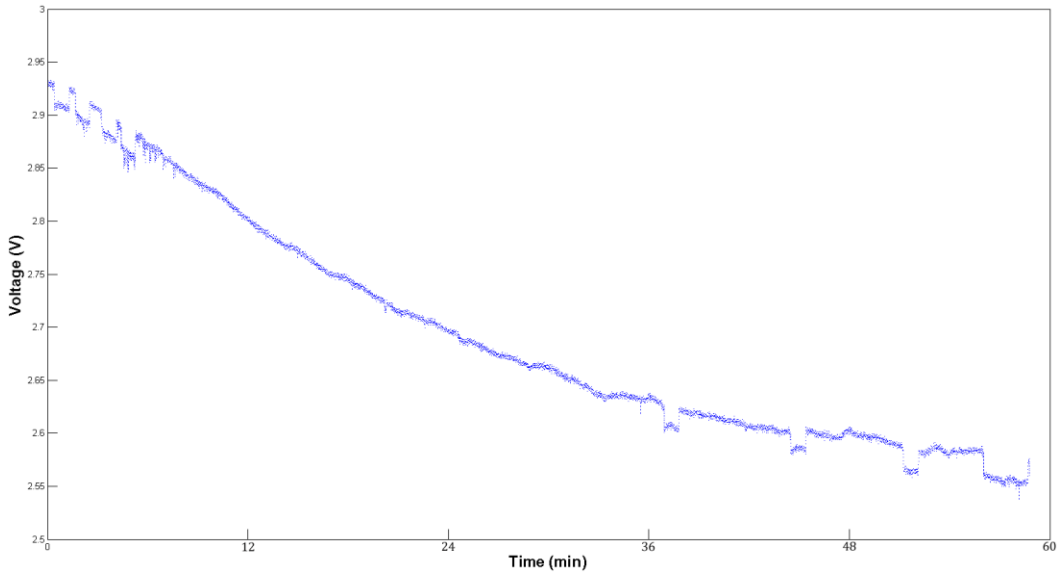


Figure 4-20 Thermal Drift

4.2.8 Crosstalk between structures

The structures on the sensors are close. This test exhibits if there are crosstalk between adjacent structures when pressure is applied on a particular structure. The result illustrates that the diagonal structures have negligible crosstalk but crosstalk shows up in four orthogonal structures. While the resistance of the structure, where pressure is applied, decreases because of inward deformation, resistance of adjacent structures increases because of outward deformation.

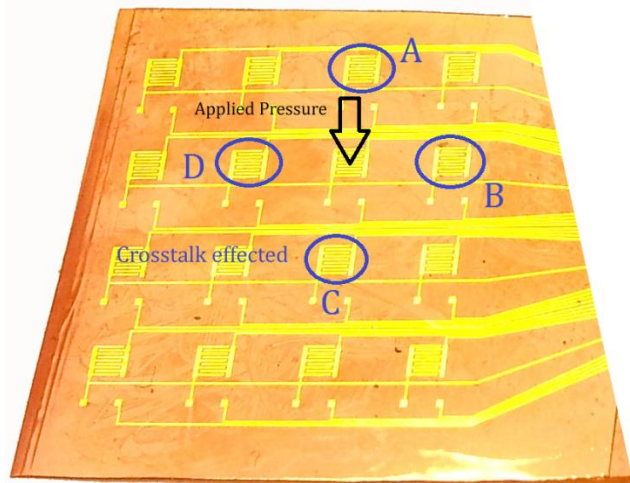


Figure 4-21 Crosstalk between sensors

Table 4-6 Crosstalk between sensors

Center Sensor reading (raw)	Crosstalk reading				Average	Percentage
	A	B	C	D		
640.13	595.23	596.31	597.6	598.29	596.86	6.76%
633.24	589.43	590.71	592.2	593.95	591.57	6.58%
618.02	592.24	591.17	592.15	592.61	592.04	4.2%

4.2.9 AC Response

All the tests above, we measured DC response of the sensor. This test illustrates how the sensor respond with an AC input. The applied pressure followed a sinusoidal trajectory increasing from zero to 1lb with a frequency of 1Hz. The experiment was conducted on 12 IDE structures for three times each. Some of the results are shown below. A moving average filter was used with a window of 10 samples, on the sensor response.

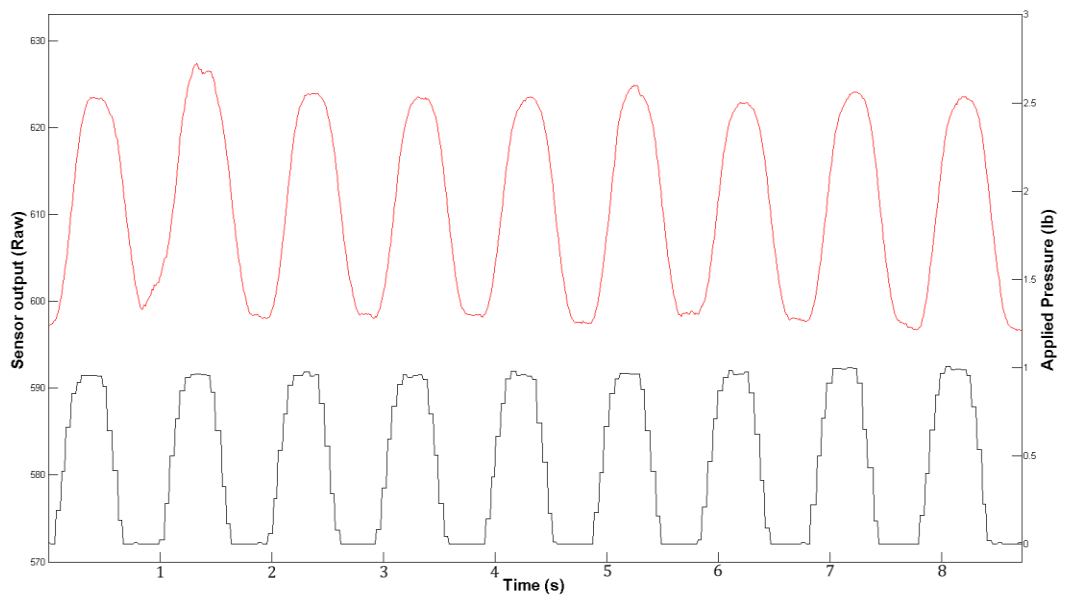


Figure 4-22 Ac response of structure 1

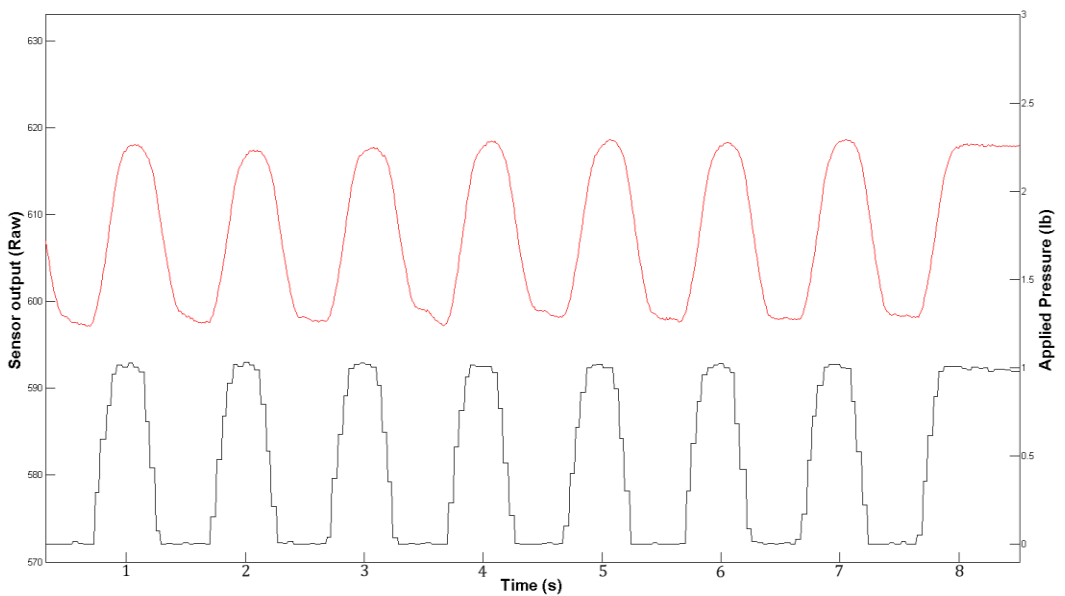


Figure 4-23 Ac response of structure 6

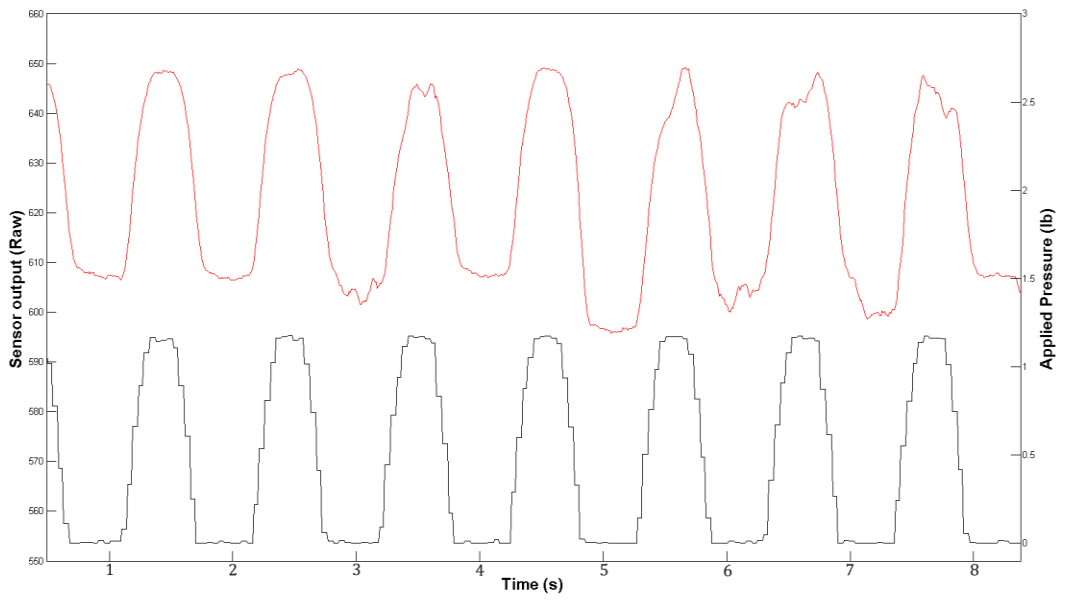


Figure 4-24 Ac response of structure 11

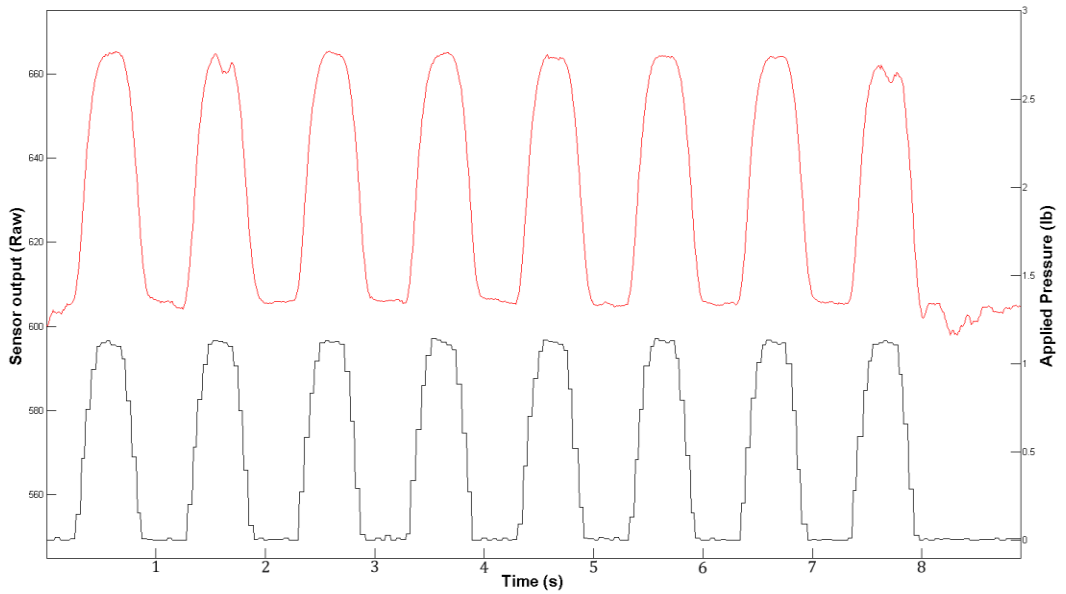


Figure 4-25 Ac response of structure 16

Chapter 5

Applications of Robot Skins to Robotics and Prosthetics

Allowing robots to sense exterior force, temperature and proximity can improve their awareness of surroundings make them safer to be around which in turn enhance the quality of human-robot interaction. In this chapter, we prototyped robot skins with off-the-self sensors and placed those on two different platforms. Several experiments were conducted to validate the robot skin's necessity for better quality of HRI. This chapter is organized as follows: Section 5.1 describes work of an intuitive interaction for personal robots by integrating multimodal sensors along with a HMI framework into a Kuka YouBot®. Section 5.2 introduces a teleoperated interface to control a powered prosthetic hand using a tracking glove that has pressure sensors.

5.1 YouBot – A Mobile Manipulator with HRI

YouBot®, from Kuka Industries, is an omnidirectional mobile platform with five degrees of freedom manipulator and two-finger gripper attached to it, made specifically for research institutes and universities, where they can easily implement their own controller and application ideas with the robot. Our primary target was to explore Physical Human-Robot Interaction (pHRI) applications.

As robots are started to excel from confined factory areas to almost everywhere, inevitability of physical human-robot interaction rises and so does safety concerns. Task that requires dyad effort in a shared workspace, robots need to perceive human intent. Though recent research use vision systems extensively, but pHRI requires rapid and real-time response. Despite of all the advantages visual servo

system has, its performance is restricted by the processing delay from camera. To address this issue, three infrared sensors have been used as a low cost alternative of identifying basic objects along with proximity. With each sensor covering $\sim 45^\circ$, we have a field of view of 120° . Processing infrared data is faster compared to an image-processing task.

When it comes down to human safety only one set of awareness of the surrounding environment is not adequate. A large portion of human body is covered with skin that can sense temperature, touch, and force. Such a large sensory system is also required for robots if we want to increase the effectiveness of the pHRI system. Only vision is not sufficient to interact with the environment. Robot's perception of environment can be improved with the distributed sensor skin, which in turn improve the performance of pHRI. Therefore, four piezo-resistive force sensors was placed on the robot in order to interpret haptic communication from human in the sense of pushing force. Based on the manipulator's link axis and applied force's axis robot base will move on 2D surface and manipulator on 3D space. Resulting movement will always be parallel to the applied force direction.

KUKA YouBot has an onboard pc running Robot Operating System (ROS) to control the base and manipulator. For real-time close-loop control a hardware device, called roboRIO, from National Instrument, has been used to collect infrared and force sensors' information.

5.1.1 Sensors

5.1.1.1 IR Sensors

Omron's MEMS Thermal Sensor, D6T-44L (Fig. 5-1), has high SNR, superior noise immunity, high-precision area temperature detection with low cross-talk field of view characteristics [38] and small form factor (14mm x 18mm). I2C bus was used to communicate with this sensor. The sensor provides 4x4 pixel data (Fig. 5-2).



Figure 5-1 Omron D6T-44L [38]

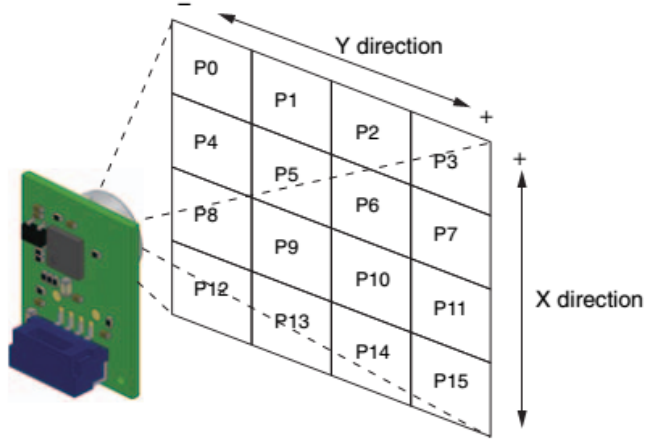


Figure 5-2 Field of view divided into 4-by-4 pixels [38]

This sensor has advantages over conventional pyroelectric sensors that is unable to detect a stationary object. This is because that type of sensors can only detect the change of signal. In addition, D6T-44L continually detects the far-infrared ray of an object, while the pyroelectric models do not [38].

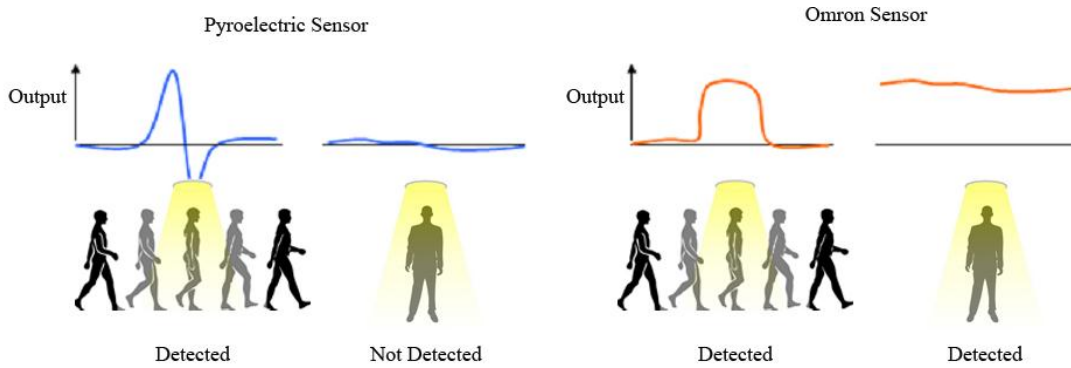


Figure 5-3 Difference between pyroelectric and Omron senor

Each sensor has a view angle of 45° . With three sensors, 4×12 pixels will cover approximately 120° with some overlapping.

5.1.1.2 Interfacing IR sensors

I²C communication protocol is a two-line bus and can support up to 128 devices, using 7-bit addressing scheme. Therefore, I²C devices should have unique address to differentiate between them. Omron D6T-44L comes with a fixed address. In order to use more than one sensor using same I²C bus we need an I²C bus switch. Furthermore, the sensor uses 5V TTL line whereas the real-time hardware we are using (roboRIO) uses 3.3V TTL line. Therefore, along with an I²C bus switch we also need a level translator. Texas Instrument's PCA9546A is a quad bidirectional translating switch. This will serve both of our purposes.

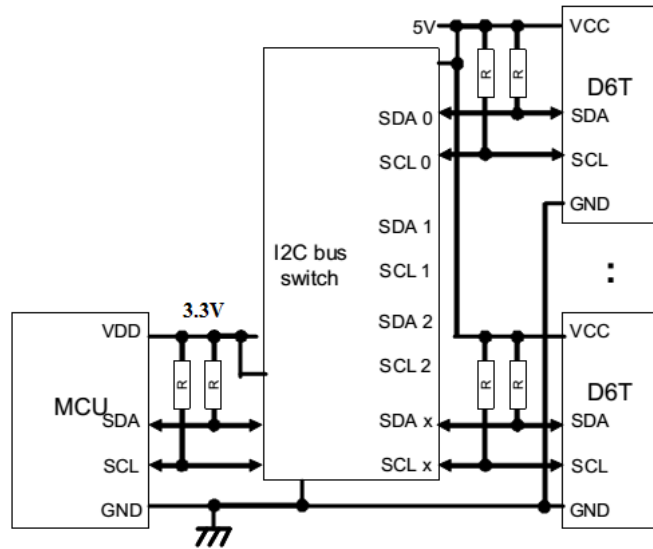


Figure 5-4 Functional block diagram of sensor interfacing [39]

An output from three sensors is shown in a heat map (Fig. 5-5). Dark areas are cold in nature and bright areas represent high temperature.

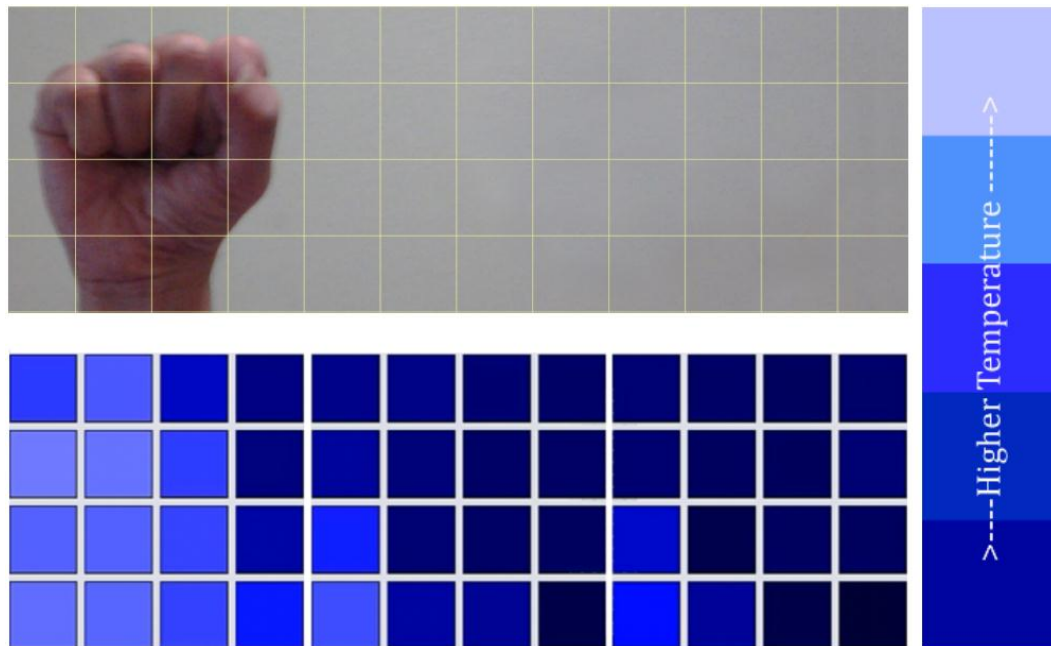


Figure 5-5 IR sensors' output in 12x4 pixel

This information can be used to detect the distance of an object. If an object is near it will cover most of the field of view of the sensors. All the pixels will show the presence of an object in their area. If an object is far away from the sensors, a few pixels will detect an object's presence. Fig. 5-6 IR intensity of all 16 pixels with respect to distance over the span of 3ft, by moving the object away from the sensors, about 0.5 ft. in each iteration.

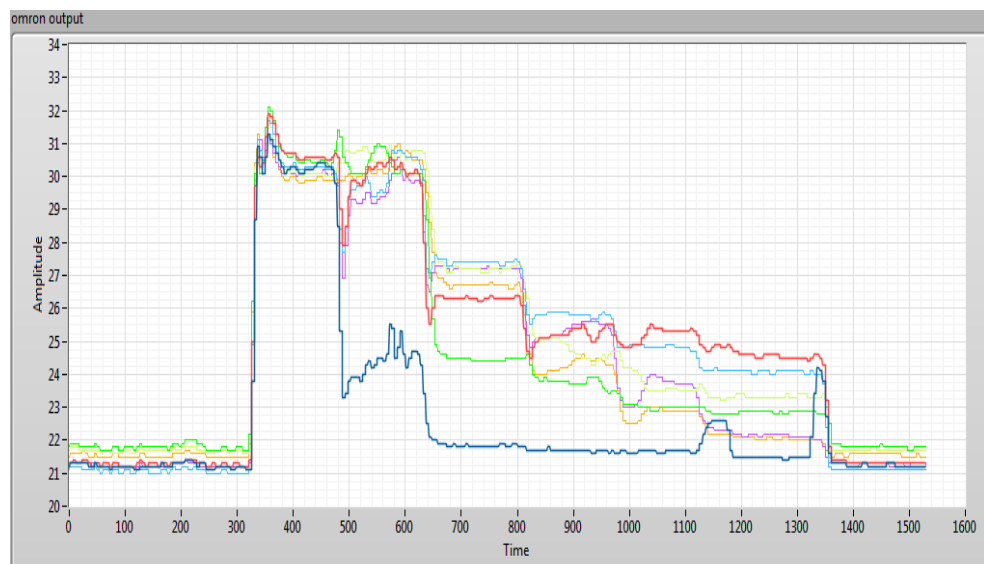


Figure 5-6 IR intensity Vs time for 16 pixels

5.1.1.3 Pressure Sensors

Tekscan's off-the-self piezoresistive Flexiforce pressure sensor (Fig. 5-7) has superior linearity & accuracy ($\pm 3\%$). They are cost effective and durable enough to stand up to most environments. The resistance change from infinity to $\sim 50K$ with maximum 5- μ sec response time and can handle up to 100lbs. The sensor is built around a thin and flexible substrate. When pressure is applied on the round area, resistance changes. The overall length of the sensor is about 2.25".



Figure 5-7 Tekscan's Flexiforce Sensor

Usually a series resistor is used with these sensors to create a voltage divider. Depending on the force applied on the sensor, voltage across series resistor will change. In order to find an optimal resistor, we used:

$$\left(\frac{f(x)}{g(x)}\right)' = \frac{f'(x) \cdot g(x) - f(x) \cdot g'(x)}{g^2(x)} \quad (5-1)$$

The difference $V_{MAX} - V_{MIN}$ has an extremum:

$$\frac{d}{dR_x} \left(\frac{R_{MAX}}{R_{MAX} + R_x} - \frac{R_{MIN}}{R_{MIN} + R_x} \right) = 0 \quad (5-2)$$

Solving for R_x gives

$$R_x = \sqrt{R_{MAX} \cdot R_{MIN}}$$

5.1.1.4 Interfacing Pressure Sensors

Mean force a human can exert with one hand is around 45lbs [41]. In order to measure between zero and 50lbs, formula yields a resistor value of $1.8M\Omega$. RoboRIO's analog channel can handle up to $10K\Omega$ input impedance, whereas our system will exert more than $1M\Omega$. Emitter buffer (Fig. 5-8) was used to reduce the input impedance.

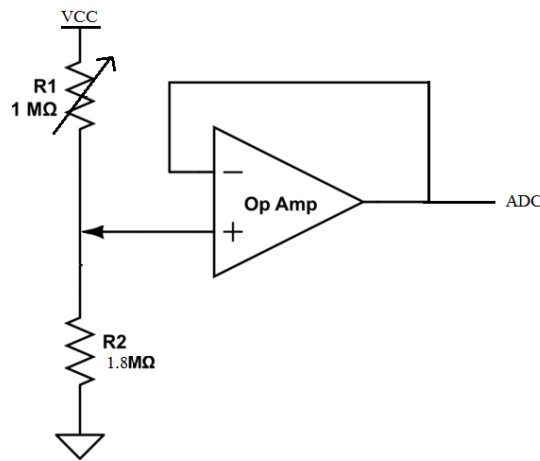


Figure 5-8 Interfacing schematic for a sensor

Texas Instrument is TL274, a package of quad operational amplifiers, was used for this purpose. Sensors were placed on the four sides of the youBot gripper. P10 polymer was placed on top of the sensors to mimic skin.

5.1.2 Casing

A PCB was designed to accommodate all the interfacing electronics in one board. There are three distinct sections on the board. Power supply, IR sensor interface and force sensor interface. YouBot can provide 24v, but board needs 5v and 3.3v. Power regulator was used to generate required voltages for the board. The board, the IR sensors and all the connecting wires are encased in a 3D printed box as shown in Fig. 5-10.

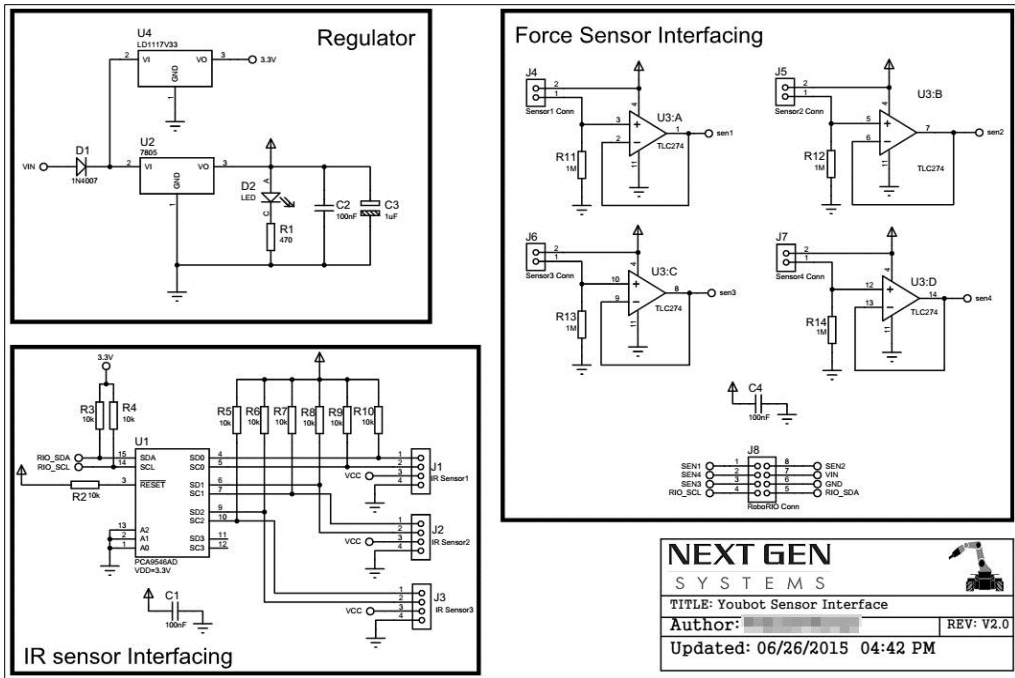


Figure 5-9 Schematic diagram of sensor interfacing board





(b)

Figure 5-10 (a) Inside the case (b) After enclose everything inside

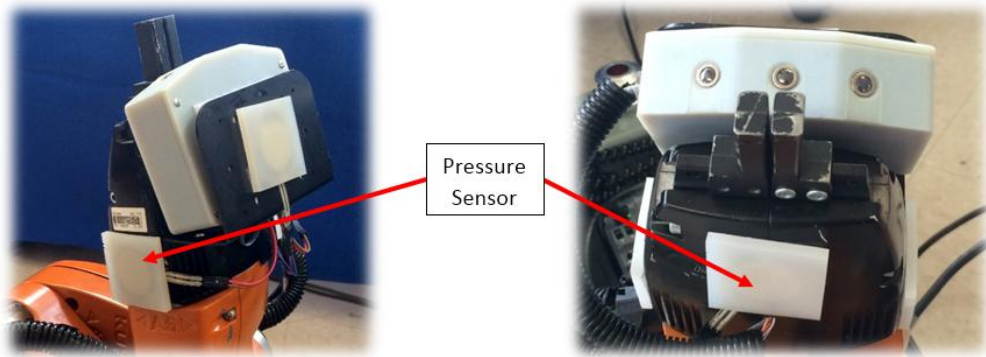


Figure 5-11 Sensor placed on youBot

5.1.3 Real-Time Hardware

National instruments' roboRIO, the new NI reconfigurable I/O (RIO) controller built just for robotics application. It is faster, smaller, robust and more powerful than previous controllers. It features a user-programmable FPGA and a 667 MHz dual core Real-Time processor, both of which are Xilinx Zynq chipset. It is running NI Linux Real-Time OS and can be programmed with the graphical programming tool, LabVIEW, an easy-to-use programming interface. A simplified block diagram of the hardware system architecture is shown in Fig. 5-12. The LabVIEW code has been written in real-time structure (Fig. 5-13). Pressure sensors

reading loop were generating data after every 1ms whereas infrared sensors were generating after every 30ms. Then all the data were placed in one String type variable. This information then relayed back to the ROS machine of youBot.

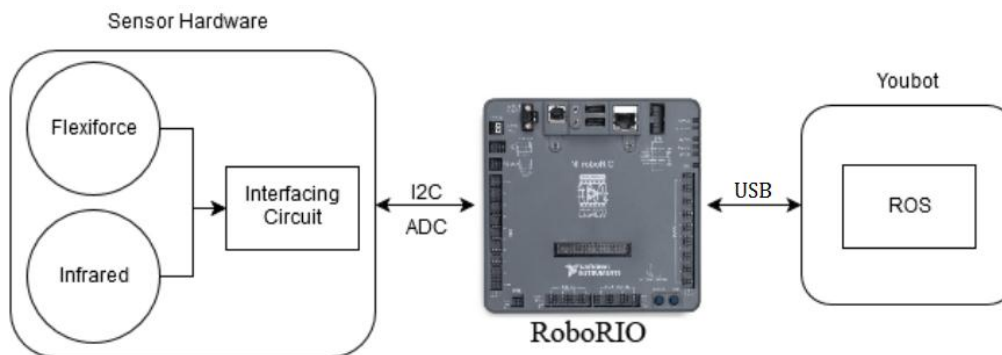


Figure 5-12 System diagram of real-time hardware

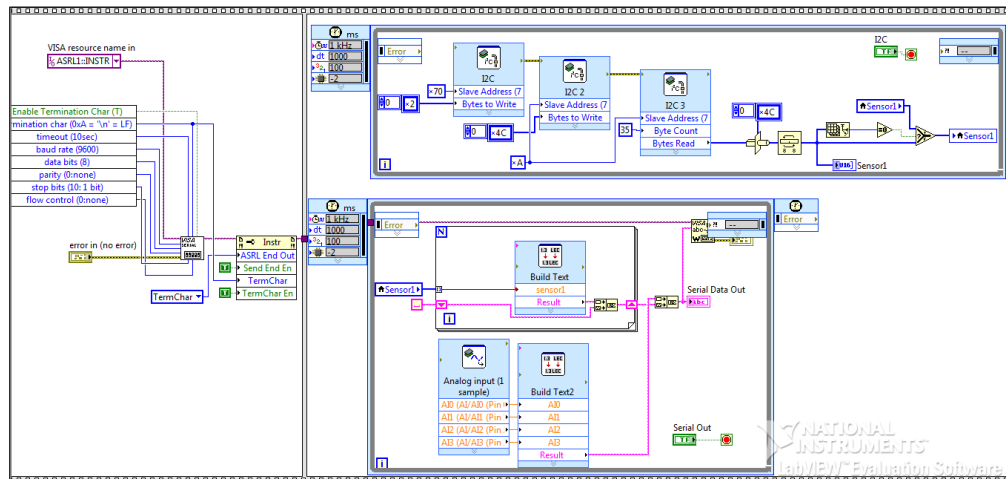


Figure 5-13 Snippet of the code

5.1.4 Software Framework

The framework has three distinct sections. Data collection and processing, transformation of the sensor data into desired manipulator angle and base velocity, command the youBot controller to achieve desired orientation.

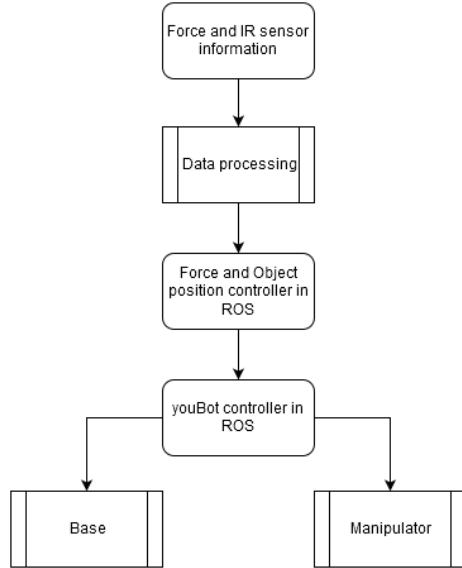


Figure 5-14 Block diagram of the software framework

YouBot has an onboard mini ITX PC-Board with embedded CPU, 2 GB RAM, running Ubuntu 12.04 [42]. It has a high level C++ API as well as low-level control of the robot. It also supports ROS (Robot Operating System) Hydro and provides a ROS wrapper based on the C++ API. A ros node was written to process the sensor data and generate control messages for the manipulator and base. RoboRIO directly publish data into two topics. A subscriber fetch those data and process it to create manipulator position angle and base velocity, and publish it to a topic whose subscriber is robot controller node. Kinematics calculations are handled by ROS. Two libraries are used to calculate the transformation matrix from axis to axis, "tf" (i.e. transformation) and "KDL" (i.e. Kinematics and Dynamics Library).

5.1.5 Guidance Experiments

The experiment was conducted on expert and non-expert subjects. Non-expert subjects were those who had no prior experience of the robot or its

functionality. Both of those subjects were asked to physically guide youBot on the lab floor, and pick up objects. In each case, we recorded accuracy and completion time of move and pick tasks along the way. To create a rigorous method of testing the desired path, several way points are selected on the lab floor as indicated in Fig. 5-15. Distances between waypoints were approximately 10 ft. each. The task objective given to the operator is to acquire fuzzy green compliant toys with the gripper, transport it to different waypoints and release it.

Two types of experimental trials were conducted, including teleoperation via tablet and direct physical interaction (or Manikin mode) via the skin sensors to find out the intuitive interface among both expert and non-expert users. Specifically, the user was required to accomplish the following tasks:

1. Pick up initial object
2. Transport object to waypoint
3. Deliver object in proximity (2-3 inches) from waypoint item
4. Pick up next object
5. Proceed to next waypoint
6. Deliver final waypoint item into a bin

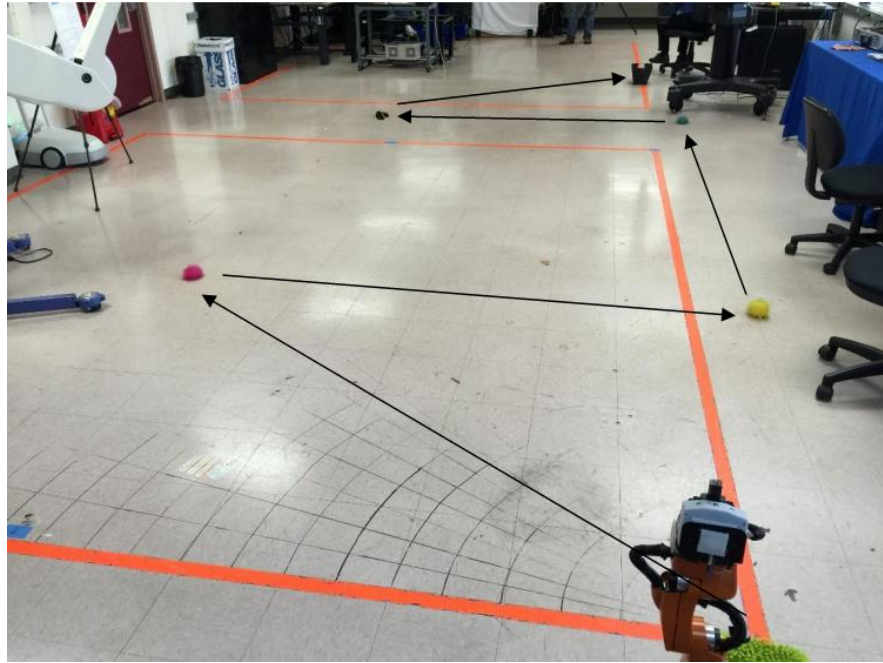


Figure 5-15 Time test path for youBot

In teleoperation mode, a virtual joystick pivot controlled the motion of the base, while the arm was controlled through a Cartesian controller using tilt angles from the tablet. The user was able to open and close the grippers using a button located on a custom Android tablet application. The time taken to traverse the course was recorded for several expert and non-expert users, and five tests per subject were performed to obtain consistent results with respect to desired location. Base robot localization was accomplished using the internal odometer, including a custom installed LIDAR sensor, internal wheel encoders, and can be visualized in RVIZ. The arm was localized with respect to the base given good quality joint encoders on the youBot.

The timed trial data was tabulated as shown in Table 5-1 for a few expert and non-expert users after processing it from a rosbag file. It can be seen that in teleoperation mode, the common task completion time for an experienced user was 2.5-3 minutes. However, the non-expert users took longer, between 5.7- 7 minutes to complete the desired tasks. The time difference for both non-users and expert users required to operate the robot with the two different interfaces is minimal. In addition to completion times, we recorded the location information during interaction with users. The positions of the robot during experiments were updated with respect to the room using the LIDAR sensor and internal odometer. Figures 5-16 and 5-17 summarize the trajectories obtained via manikin and tablet control, respectively.

Table 5-1 Task completion times in 20 youBot experiments

Test Type	Expert User 1	Expert User 2	Non-expert User 1	Non-expert User 2
Tablet Control	2 min 55 sec	3 min 8 sec	6 min 35 sec	6 min 08 sec
	2 min 38 sec	2 min 54 sec	6 min 28 sec	5 min 43 sec
	2 min 42 sec	2 min 39 sec	6 min 22 sec	5 min 40 sec
	2 min 33 sec	2 min 21 sec	6 min 10 sec	5 min 48 sec
	2 min 28 sec	2 min 19 sec	6 min 12 sec	5 min 30 sec
Manikin Control	2 min 58 sec	3 min 1 sec	6 min 49 sec	6 min 38 sec
	2 min 49 sec	2 min 56 sec	6 min 41 sec	6 min 22 sec
	2 min 51 sec	2 min 39 sec	6 min 42 sec	6 min 29 sec
	2 min 53 sec	2 min 50 sec	6 min 33 sec	6 min 21 sec
	2 min 46 sec	2 min 42 sec	6 min 39 sec	6 min 35 sec
Avg. Teleop Control	2 min 39 sec	2 min 40 sec	6 min 23 sec	5 min 46 sec
Avg. Manikin Control	2 min 51 sec	2 min 49 sec	6 min 41 sec	6 min 29 sec

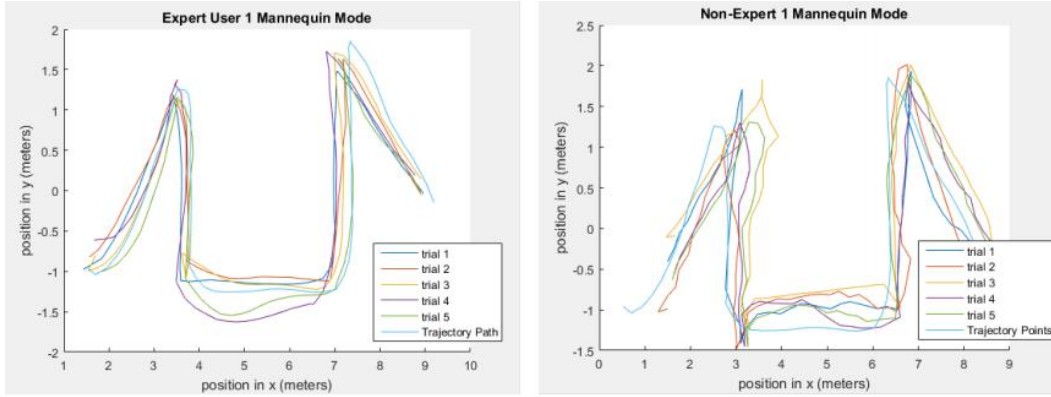


Figure 5-16 youBot Cartesian position during manikin control

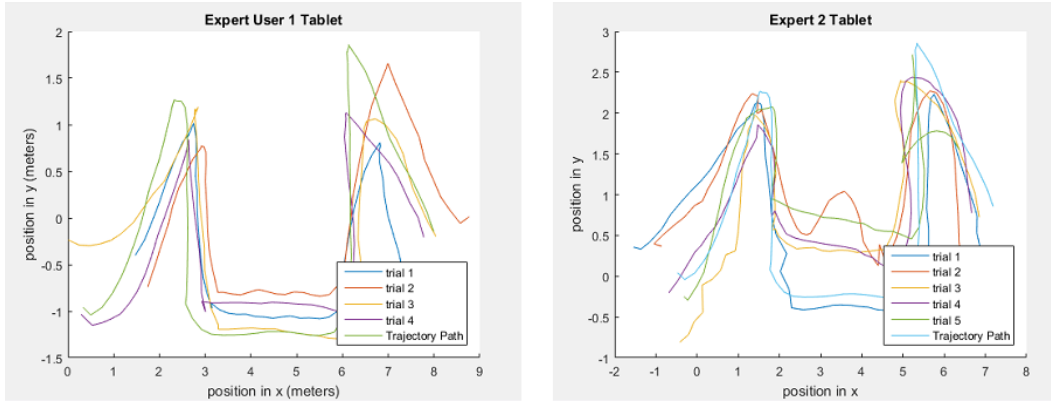


Figure 5-17 youBot Cartesian position during tablet control

By general inspection of the base trajectories, one can infer that the manikin mode is more accurate than teleoperation with a tablet, and that the differences between expert and non-expert users are not significant. We demonstrated basic capabilities to acquire interaction data from users, which will pave the way for larger user studies in the future [42]. Data collected, and in particular, arm trajectories are still being analyzed, but we have drawn the following preliminary conclusions when comparing the interfaces:

- 1) The physical interaction (or manikin) guidance results in the most accurate robot trajectories for both expert and non-expert users.
- 2) Expert users can complete pick and place manipulation and mobility tasks significantly faster than non-expert users, indicating that these interfaces are not very intuitive to use.

5.2 RoboLimb – A Prosthetic Hand

Prosthetic hands have been around for decades. Nowadays robotic prosthetic limbs come with multiple degrees of freedom fingers. But the problem arises with the amount of control channels available with the biological signal from EMG or similar kind of sensors [63][64]. It restricts the usability of such dexterous prosthetic limbs. In the realm of virtual reality world, people have been using something called “digital glove” to interact with virtual object in real time. In this work, we combine the both technology to help unilateral amputees who has one sound hand and can teleoperate the prosthetic hand.

5.2.1 Hardware Setup

The tracking glove is consists of six flexion sensors [65], from Spectra Symbol, the resistance of which changes when they are flexed. They are sewed on to the finger sleeves so that we can track the bending of the fingers. The sensors are connected with an electronic hardware that has a microcontroller to measure the resistance change of the sensors in the means of voltages and provide that information to Raspberry Pi [66]. Ras-Pi is used to communicate with the prosthetic hand, from Touch Bionics [67], through CAN bus. A separate power supply board was designed

to provide power to the data acquisition board of the sensors, Raspberry Pi and Prosthetic Hand.

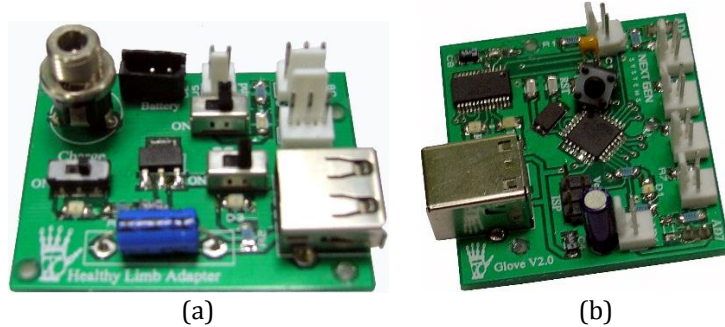


Figure 5-18 (a) Power supply board (b) Data acquisition board

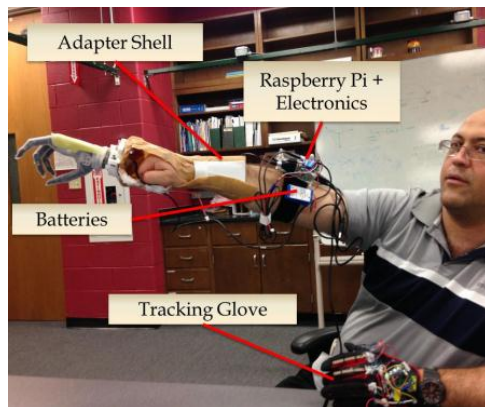


Figure 5-19 RoboLimb [68]

5.2.2 Testing and Results

The experiment was conducted on three non-impaired volunteers. They were asked to do four tasks. This is detailed in [68].

- a) Pick up a large object using both sound hand and prosthetic hand.
- b) Pick up a pen using pinch grip.
- c) Pick up a water bottle and drink from it.
- d) The Box and Blocks test [69]

The users were able to perform all the tests as instructed. The Box and Block exhibits that it is possible to move $9(\pm 1)$ blocks per minute. Overall preliminary results shows that controlling prosthetic hand is faster with the glove compared with the mobile app control for the same prosthetic hand

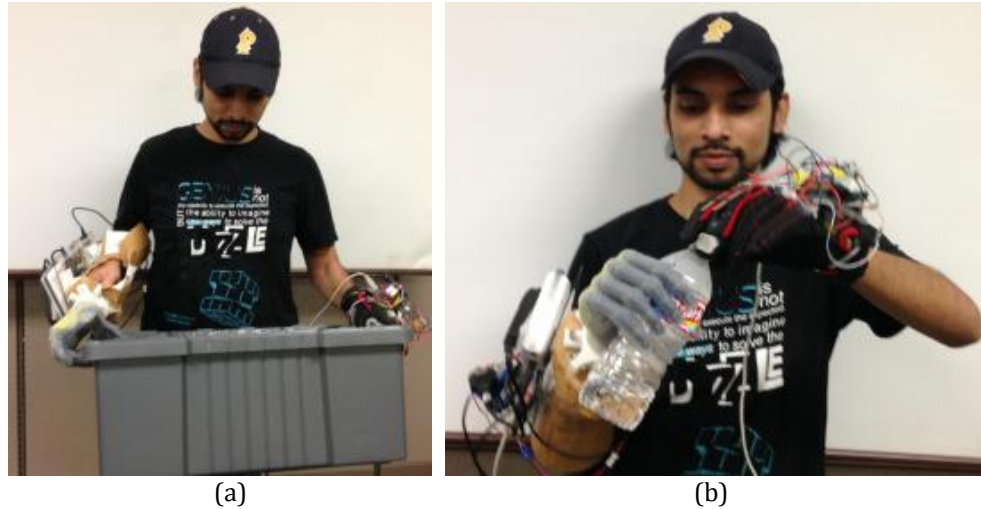


Figure 5-20 A subject (a) Carrying a heavy box (b) Picking up a water bottle

Chapter 6

Conclusions

6.1 Conclusion

Robot applications are increasing in every nature of human life. As it expands rapidly so does safety concerns, for human and for robot itself. Once the robots get out of the structured space of factories the world is full of dynamic environments. It is no more possible to pre-program everything in advance. The robots need to perceive and adapt to its surroundings by themselves with the help of sensors. Robotic skin integrated with multi-modal sensors can work wonders in this case. It will provide real time sensory information that will make human-robot coexistence safe and help robots to operate in non-structured environment.

6.1.1 Sensor Manufacturing Technology

The current semiconductor manufacturing technology is not suitable for robot skin with multi-modal sensors embedded in it. However, EHD Inkjet printing technology can address all the issues that conventional technology cannot. This method depends on several parameters. After considerable of testing and experimenting these are fixed to have an optimal and scalable sensor manufacturing process.

6.1.2 Automated Printing

Previously, the printing tasks was operated by G-code, which required manual alignment and can print only one structure at a time. To increase the throughput we need auto calibration process along with a way to print on more than

one structure at a time. LabVIEW was used to control the XYZ stage that solved these issues.

6.1.3 Sensor Characterization Methodology

Every sensor that come out of industries goes through a characterization and calibration process. It should not be different for our sensors too. A proper methodology was required to test these sensors. Our sensor can sense pressure and in nature act as strain gauge. Therefore, a set of experiments were listed in the methodology that test the response of the sensor against some pre-determined parameters.

6.1.4 Pressure Sensor Application on Robots

Electronic sensors are the primary method for robots to gather information about their surroundings. There are many types of sensors that have been exploited in robotics already, including vision, vibration, temperature, infrared etc. to name a few, and have been routinely used to reduce uncertainty for robots in a dynamic and unstructured environment. Some of the experiments were conducted with pressure sensors.

6.2 Future Work

6.2.1 Sensor Manufacturing Optimization

Future work will involve parameter optimization for other inks that showed preliminary promising results.

6.2.2 Automated Printing

The automation of printing can handle a single sensor array that consists of 16 single interdigitated structure. Future work will involve the expansion of this to cover a whole wafer of sensors.

6.2.3 Sensor Testing Methodology

The set of experiments conducted on the sensors were done manually, one at a time. It is possible to automate the whole system. This will be done in the future.

6.2.4 Sensor's Application on Robots

For this thesis, we tested the application on youBot and RoboLimb. Future work will include more robots with pressure sensing applications.

References

- [1] R. S. Dahiya, G. Metta, M. Valle and G. Sandini, "Tactile sensing—from humans to humanoids," *IEEE Transactions on Robotics*, vol. 26, no. 1, pp. 1-20, 2010.
- [2] C. C. Kemp, A. Edsinger and E. Torres-Jara, "Challenges for Robot Manipulation in Human Environments," *IEEE Robotics and Automation*, vol. 14, no. 1, pp. 20-29, 2007.
- [3] J. Rajruangrabin and D. O. Popa, "Enhancement of Manipulator Interactivity through Compliant Skin and Extended Kalman Filtering," in *Automation Science and Engineering, 2007. CASE 2007. IEEE International Conference on*, Sept. 2007, pp. 1111-1116.
- [4] B. D. Argall and A. G. Billard, "A survey of Tactile Human-Robot Interactions," *Robotics and Autonomous Systems*, vol. 58, no. 10, pp. 1159-1176, 2010.
- [5] Westling, G., and R. S. Johansson. "Factors influencing the force control during precision grip." *Experimental Brain Research* 53.2 (1984): 277-284.
- [6] H. Sakoe and S. Chiba, "Dynamic programming algorithm optimization for spoken word recognition," *Acoustics, Speech and Signal Processing, IEEE Transactions on*, vol. 26, no. 1, pp. 43-49, Feb. 1978.
- [7] F. Itakura, "Minimum prediction residual principle applied to speech recognition," *Acoustics, Speech and Signal Processing, IEEE Transactions on*, vol. 23, no. 1, pp. 67-72, Feb. 1975.
- [8] E. Keogh and C. A. Ratanamahatana, "Exact indexing of dynamic time warping," *Knowledge and Information Systems*, vol. 7, no. 3, pp. 358-386, 2005.
- [9] "Programmed to Treat Autism," 2011. [Online]. Available: <http://texasmrc.org/programmed-to-treat-autism/>.
- [10] I. Ranatunga, N. A. Torres, R. Patterson, N. Bugnariu, M. Stevenson, D. O. Popa, and F. Worth, "RoDiCA: a Human-Robot Interaction System for Treatment of Childhood Autism Spectrum Disorders," in *Proceedings of the 5th International Conference on Pervasive Technologies Related to Assistive Environments*, ser. PETRA '12. New York, NY, USA: ACM, 2012.
- [11] N. A. Torres, N. Clark, I. Ranatunga, and D. Popa, "Implementation of Interactive Arm Playback Behaviors of Social Robot Zeno for Autism Spectrum Disorder Therapy," in *Proceedings of the 5th International Conference on Pervasive Technologies Related to Assistive Environments*, ser. PETRA '12. New York, NY, USA: ACM, 2012, p. 1.
- [12] "What Is NI myRIO?", 2016. [Online]. Available: <http://www.ni.com/myrio/what-is/>
- [13] "Kinect: Gestures," [Online]. Available: <http://support.xbox.com/en-US/browse/xbox-360/kinect/Gesture>.

- [14] Chen, C.-H., Saville, D. A., and Aksay, I. A., "Scaling laws for pulsed electro-hydro-dynamic drop formation," *Applied Physics Letters* 89, 12410, 2006.
- [15] Lee, D.-Y., Lee, J.-C., Shin, Y.-S., Park, S.-E., Yu, T.-U., Kim, Y.-J. and Hwang, J., "Structuring of conductive silver line by electrohydrodynamic jet printing and its electrical characterization," *Journal of Physics: Conference Series*. Vol. 142. No. 1. IOP Publishing, 2008.
- [16] Sidhu, R., Sin, J., Lee, W. H., Stephanou, H. E., and Wijesundara, M.B.J., "Electrohydrodynamic printing of metal oxide microstructures," *International Conference On Micromanufacturing*, pp. 458-461, 2012
- [17] Chatzandroulis, S.; Goustouridis, D.; Normand, P.; Tsoukalas, D. "A solid-state pressure-sensing microsystem for biomedical applications". *Sens. Actuators A Phys.* 1997, 62, 551–555.
- [18] Cheng, M.Y.; Lin, C.L.; Lai, Y.T.; Yang, Y.J. "A polymer-based capacitive sensing array for normal and shear force measurement". *Sensors* 2010, 10, 10211–10225.
- [19] Fiorillo, A.S. "A piezoresistive tactile sensor," *IEEE Trans. Instrum. Meas.* 1997, 46, 15–17.
- [20] Orthnerc, M.P.; Bueteisch, S.; Magda, J.; Rieth, L.W.; Solzbacher, F. "Development, fabrication, and characterization of hydrogel based piezoresistive pressure sensors with perforated diaphragms," *Sens. Actuators A Phys.* 2010, 161, 29–38.
- [21] Eaton, W.P.; Smith, J.H. "Micromachined pressure sensors: Review and recent developments," *Smart Mater. Struct.* 1997, 6, 530–539.
- [22] Blasquez, G.; Chauffleur, X.; Pons, P.; Douziech, C.; Favaro, P.; Menini, P. "Intrinsic thermal behaviour of capacitive pressure sensors: Mechanisms and minimization," *Sens. Actuators A Phys.* 2000, 85, 65–69.
- [23] Tressler, J.F.; Alkoy, S.; Newnham, R.E. "Piezoelectric sensors and sensor materials," *J. Electroceram.* 1998, 2, 257–272.
- [24] Barlian, A.A.; Park, W.T.; Mallon, J.R., Jr; Rastegar, A.J.; Pruitt, B.L. "Review: Semiconductor piezoresistance for microsystems," *IEEE Proc.* 2009, 97, 513–552.
- [25] Tudor, M.J.; Beeby, S.P. "Automotive pressure sensors," In *Automotive Sensors*. Turner, J., Ed.; Momentum Press: New York, NY, USA, 2009; pp. 37–84.
- [26] Chiolerio, A.; Roppolo, I.; Sangermano, M. "Radical diffusion engineering: Tailored nanocomposite materials for piezoresistive inkjet printed strain measurement," *RSC Adv.* 2013, 3, 3446–3452.
- [27] Calvert, P., Patra, P., Lo, T-C., Chen, C., Sawhney, A., and Agrawal, A., "Piezoresistive sensors for smart textiles," *Proc. SPIE 6524, Electroactive Polymer Actuators and Devices*, (2007)

- [28] Latessa, G., Brunetti, F., Reale, A., Saggio, G., and Carlo, A. D., "Piezoresistive behavior of flexible PEDOT:PSS based sensors," *Sensors and Actuators B: Chemical*, 139 (2), 304-309 (2009).
- [29] Lang, U., Rust, P., and Dual, J., "Towards fully polymeric MEMS: Fabrication and testing of PEDOT/PSS strain gauges," *Proc. Micro- and Nano-Engineering*, 1050-1053 (2007)
- [30] Takamatsu, S. and Itoh, T., "Novel MEMS Devices Based on Conductive Polymers," *Electrochemical Society, Interface*, (2012)
- [31] Das, A.N.; Ping Zhang; Lee, W.H.; Popa, D.; Stephanou, H., " μ^3 : Multiscale, Deterministic MicroNano Assembly System for Construction of On-Wafer Microrobots," *IEEE International Conference on Robotics and Automation*, 2007, Volume-Issue 10-14, Page(s):461 – 466, Roma, Italy, April 2007
- [32] "Strain Gauge Application" 2002. [Online]. Available: <http://soliton.ae.gatech.edu/people/jcraig/classes/ae3145/ae3145.html>
- [33] "Wheatstone Bridge" 2015. [Online]. Available: https://en.wikipedia.org/wiki/Wheatstone_bridge
- [34] "Instrumentation amplifier" 2016. [Online]. Available: https://en.wikipedia.org/wiki/Instrumentation_amplifier
- [35] "Butterworth Filter" 2016. [Online]. Available: https://en.wikipedia.org/wiki/Butterworth_filter
- [36] "A3200 Drive Rack" 2016. [Online]. Available: <http://www.aerotech.com/product-catalog/drives-and-drive-racks/npaq.aspx>
- [37] "Sallen-Key Topology" 2016. [Online]. Available: https://en.wikipedia.org/wiki/Sallen%E2%80%93Key_topology
- [38] "D6T MEMS Thermal Sensors Datasheet" 2016. [Online]. Available: <http://www.omron.com/ecb/products/pdf/en-d6t.pdf>
- [39] "Usage of D6T-44L Thermal sensor" 2016. [Online]. Available: https://www.omron.com/ecb/products/sensor/special/mems/pdf/AN-D6T-01EN_r2.pdf
- [40] "Flexiforce Pressure Sensor" 2016. [Online]. Available: <https://www.sparkfun.com/products/11207>
- [41] Chaffin, D., Andres, R., Garg A., "Volatile Postures during Maximal Push/Pull Exertions in the Sagittal Plane", *Human Factors*, Paper 25(5), 541-550(1983)
- [42] Rommel Alonzo, Sven Cremer, Fahad Mirza, Sandesh Gowda, Larry Mastromoro, and Dan O. Popa, "Multimodal sensor and HMI integration with applications in personal robotics," in SPIE 9494, Next- Generation Robotics II. Baltimore, MD., May 2014.
- [43] M. Wassink and S. Stramigioli, "Towards a Novel Safety Norm for Domestic Robots" in IEEE/RSJ Int. Conf. on Intelligent Robots and Systems (IROS2007), San Diego, USA, 2007, pp. 3354–3359.

- [44] K. Ikuta, H. Ishii, and M. Nokata, "Safety Evaluation Method of Design and Control for Human-Care Robots" *Int. J. of Robotics Research*, vol. 22, no. 5, pp. 281–298, 2003.
- [45] R. S. Johansson and A. B. Vallbo, "Tactile Sensibility in the Human Hand: Relative and Absolute Densities of Four Types of Mechanoreceptive Units in Glabrous Skin," *J. Physio.*, vol. 286, pp. 283-300, 1979.
- [46] K. Myles and M. S. Binseel, "The Tactile Modality: A Review of Tactile Sensitivity and Human Tactile Interfaces," Army Research Laboratory, May, 2007.
- [47] M. S. and S. H., "Thermotactile Perception Thresholds Measurement Conditions," *Ind Health*, Oct. 2002.
- [48] E. R. Kandel, J. J. Schwartz and T. M. Jessel, *Principles of Neural Science*, 4th ed., New York: McGraw-Hill Medical, 2000.
- [49] "Research | Javey Group - Electronic Skin," [Online]. Available: <http://nano.eecs.berkeley.edu/research/eskin.html>.
- [50] M. Cutkosky, R. Howe and W. Provancher, "Ch. 9: Force and Tactile Sensors," in *Springer Handbook of Robotics*, Springer Handbooks, 2008.
- [51] V. J. Lumelsky, M. S. Shur and S. Wagner, "Sensitive Skin," in *IEEE Sensors*, vol. 1, pp. 41-51, 2001.
- [52] P. Mittendorfer and G. Cheng, "From a Multi-Modal Intelligent Cell to a Self-Organizing Robotic-Skin," in *ICRA 2013*, 2013
- [53] Cannata, G., Maggiali, M., Metta, G. and Sandini, G., 2008, August. An embedded artificial skin for humanoid robots. In *Multisensor Fusion and Integration for Intelligent Systems, 2008. MFI 2008. IEEE International Conference on* (pp. 434-438). IEEE.
- [54] Y. Tenzer, L. P. Jentoft and R. D. Howe, "Inexpensive and Easily Customized Tactile Array Sensors using MEMS Barometers Chips," Harvard School of Engineering and Applied Sciences, 2012.
- [55] "TakkTile Sensor," [Online]. Available: <http://www.takktile.com/product:takkstrip>
- [56] S. Wagner, S. P. Lacour, J. Jones, I. H. Pai-hui, J. C. Sturm, T. Li and Z. Suo, "Electronic skin: architecture and components," *Physica E: Lowdimensional Systems and Nanostructures*, vol. 25, no. 2, pp. 326-334, 2004.
- [57] L. Maiolo, A. Pecora, F. Maita, A. Minotti, G. Fortunato, D. Ricci and G. Metta, "Enhanced Piezoelectric Hybrid Tactile Sensors Fully Integrated on Ultra-Thin Polyimide Substrates for Robotic Applications," in *ICRA 2013: Research Frontiers in Electronic Skin Technology*, Karlsruhe, Germany, 2013
- [58] K.-H. Choi, A. Khan, H.-C. Kim, K. Rahman, K.-R. Kwon, N. M. Muhammad and Y. H. Doh, *Electrohydrodynamic inkjet-micro pattern fabrication for printed electronics applications*, INTECH Open Access Publisher, 2011.
- [59] "Ceramics - Research." Princeton University," [Online]. Available:

- <http://www.princeton.edu/~cml/html/research/ehdp.html>.
- [60] "ijetae," [Online]. Available: <http://www.ijetae.com/files/Volume4Issue5/>.
 - [61] National Instruments, "Real Time CompactRIO," 19 03 2014. [Online]. Available: <http://sine.ni.com/nips/cds/view/p/lang/en/nid/203964>
 - [62] National Instruments, "I/O Modules, NI 9516," [Online]. Available: <http://sine.ni.com/nips/cds/view/p/lang/en/nid/206354>. [Accessed 19 03 2014].
 - [63] Cipriani, Christian, et al. "The SmartHand trans radial prosthesis." *Journal of neuroengineering and rehabilitation* 8.1 (2011): 29.
 - [64] Miller, Laura A., et al. "Control of a six degree of freedom prosthetic arm after targeted muscle reinnervation surgery." *Archives of physical medicine and rehabilitation* 89.11 (2008): 2057-2065.
 - [65] "Flex Sensor 2.2"" [Online]. Available: <https://www.sparkfun.com/products/10264>
 - [66] "What is Raspberry Pi?" [Online]. Available: <https://www.raspberrypi.org/help/what-is-a-raspberry-pi/>
 - [67] "i-limb ultra" [Online]. Available: <http://www.touchbionics.com/products/active-prostheses/i-limb-ultra>
 - [68] Yetkin, O., Sanford, J., Mirza, F., Karulkar, R., Das, S.K. and Popa, D.O., 2015. Control of a Powered Prosthetic Hand Via a Tracked Glove. *Journal of Medical Devices*, 9(2), p.020920.
 - [69] Mathiowetz, et al. "Box and block test of manual dexterity: norms for 6–19 year olds." *Canadian Journal of Occupational Therapy* 52.5 (1985): 241-2
 - [70] Ritvij Sahasrabuddhe, "Development, Testing and Characterization of Electronic Skins for Robots" M.Sc. Thesis, December 2015.
 - [71] "Zif Connector" [Online]. Available: http://www.mouser.com/ds/2/276/0541323633_FFC_FPC_CONNECTORS-295510.pdf
 - [72] "P-10 RTV Silicone Rubber" [Online]. Available: <http://www.silicones-inc.com/index.php/about/product-datasheets/addition-cure-silicone-products-data-sheets/>
 - [73] "How to calculate Trendline" [Online]. Available: <http://classroom.synonym.com/calculate-trendline-2709.html>

Biographical Information

Fahad Mirza was born and raised in Dhaka, Bangladesh. He earned his Bachelor degree in Electrical and Electronics Engineering from Ahsanullah University of Science and Technology, Dhaka, Bangladesh in 2009. He worked for Pi Labs Bangladesh Ltd. for three years as an Embedded Firmware Engineer before he started to pursue his M.Sc. in Electrical Engineering at University of Texas at Arlington, from 2013.

He worked as a Graduate Research Assistant with the University of Texas at Arlington Research Institute, Fort Worth, TX, USA and the Next Generation Systems Research Group, where he was responsible for embedded developments for robot application. His current research interests include intelligent systems and machine learning.